**TECHNISCHE UNIVERSITÄT WIEN**

**VIENNA UNIVERSITY OF TECHNOLOGY**

**LabSem**
LABORATÓRIO DE SEMICONDUTORES
CETUC / PUC-RIO

# DIPLOMARBEIT

## Intraband Photocurrent Measurements of Quantum Dot Structures through Monochromatic Excitation

ausgeführt am
Semiconductor Laboratory (LabSem)
an der kath. Universität von Rio de Janeiro/Brasilien

unter Anleitung von
A.o. Prof. Dr. Jürgen Smoliner

durch

**Stefan L. Dornstauder**
Hofstraße 7
3382 Roggendorf
AUSTRIA
Matrikelnummer 0226032

Wien, im März 2009

# Contents

# Abstract

The topic underlying this work is monochromatic excitation as an alternative technique to Fourier Transform Infrared (FTIR) spectroscopy to perform intraband photocurrent measurements on quantum dot infrared photodetectors (QDIPs) with the purpose to investigate nonlinear effects and the sign of the photocurrent. One precondition for FTIR photocurrent spectroscopy measurements is that the measured detector must be linear. This presumption could be broken by an Auger effect, acting as a nonlinear effect.

The main challenge of the work was to design the experimental setup of the intraband measurement system with a black body source using lenses and mirrors to optimize the throughput of the monochromator.

The samples under investigation consist of ten layers of InAs quantum dots (QDs) grown on InGaAlAs lattice matched to InP substrate with three different doping levels. The samples showed a peak at around $6.6\mu m$ in the FTIR measurements. In addition to the intraband photocurrent also interband photocurrent and dark current measurements were done.

Also a theoretical background overview of QDs and QDIPs is given. Furthermore the evolution in general of photodetectors over the past decades is shown and a course roadmap is given by demonstrating that QDIPs are very appealing for mid and far infrared detector applications.

# Kurzfassung

Gegenstand der vorliegenden Arbeit ist monochromatische Anregung zur Messung von intraband Fotostrom in Infrarot-Fotodetektoren basierend auf Quantenpunkten (Quantum Dot Photodetectors, QDIP). Dies dient zur Untersuchung von nichtlinearen Effekten und der Ermittlung der Richtung des Fotostromes. Dieses Messverfahren kann als zusätzliche Analysemethode zur Infrarotspektroskopie (Fourier Transform Infrared Spectroscopy, FTIR) angesehen werden. Eine Bedingung für die Verwendung von FTIR ist, dass sich der zu untersuchende Detektor linear verhält. Diese Vorbedingung könnte durch einen in der Halbleiterprobe stattfindenden Auger Effekt verletzt werden.

Der Hauptbestandteil dieser Arbeit war der Versuchsaufbau des intraband Messsystems, bestehend aus einem schwarzen Strahler und Monochromator, und die Optimierung des optischen Durchsatzes.

Die zu untersuchenden Proben bestehen aus 10 Schichten InAs Quantenpunkten (Quantum Dots, QDs) gewachsen auf InGaAlAs welches gitterangepasst zu dem InP Substrat ist. Proben mit drei verschiedenen Dopingraten zeigten ein Fotostrommaximum bei 6,6µm in den FTIR Messungen. Zusätzlich zu den Messungen des intraband Fotostrom wurden auch Messungen des interband Fotostrom und Dunkelstrom durchgeführt.

Theoretische Grundlagen behandelnd QDs und darauf basierende Infrarot - Fotodetektoren werden ebenfalls behandelt. Weiteres wird ein Überblick der Evolution von Fotodetektoren gegeben und gezeigt, dass QDIP sehr vielversprechend für zukünftige Detektoranwendungen im infraroten Bereich sind.

# Resumo

A tese trata de um estudo de excitação monocromática como alternativa para espectroscopia de infravermelho (Fourier Transform Infrared Spectroscopy, FTIR) para medição de fotocorrente intrabanda em fotodetectores baseados em pontos quânticos (Quantum Dot Photodetector, QDIP) com o objetivo de investigar efeitos não lineares e o sinal de fotocorrente. Uma condição para utilizar espectroscopia FTIR é que o detector deve ser linear. Condição que pode ser violada por efeito Auger.

O tema principal deste trabalho foi o desenvolvimento do sistema experimental para medir fotocorrente intrabanda usando principalmente uma fonte de radiação de corpo negro e um monocromador. A maximização do sinal de saída óptico deste sistema também foi investigada.

As amostras investigadas consistem em 10 camadas de pontos quânticos (Quantum Dots, QDs) de InAs fabricados sobre InGaAlAs casado com substrato de InP. Amostras com três dopagens diferentes mostraram um pico de fotocorrente em 6.6μm nas medidas com FTIR. Adicionalmente às medidas de fotocorrente intrabanda, medidas de fotocorrente interbanda e de corrente de escuro foram feitas.

Além disto, uma visão teórica sobre QDs e QDIPs é dada. E discute-se também a evolução de fotodetectores nas últimas décadas e a razão pelo qual QDIPs são muito interessantes para uso no infravermelho no futuro.

# Chapter 1

# Introduction

This work has been done in the Semiconductor Laboratory (LabSem) at the Catholic University of Rio de Janeiro (PUC Rio) in Brazil in cooperation with the Solid State Electronics Institute of the Vienna University of Technology in Austria.

## 1.1 Motivation

Infrared photodetector, specially operating in the two atmospheric transmission windows in the 3-5μm range in mid-wave infrared (MWIR, 3-8μm) and 8-12μm range in long-wave infrared (LWIR, 8-15μm), are of great interest for many applications such as free space optical communication, toxic gas detection, night vision cameras, battle recognition systems, chemical spectroscopy and medical or biological image recognition.

It should be pointed out, that bodies whose temperatures are between 100 and 300K emit quite a large number of photons. The importance of this temperature range is, that even without any heating such objects can be detected by collecting the emitted infrared radiation. One practical application is night vision where even in the dark (when human vision is poor) cold objects can be "seen" [1].

The mid-infrared region contains also the fundamental fingerprint absorption bands of a number of pollutant and toxic gases like methane (3.3μm), $CO_2$ (4,2μm), CO (4.6μm), NOx (6.5μm) and SOx (7.3μm) and liquids.

In situ multi-component monitoring in a variety of different situations is required [2].

A new approach of infrared photodetectors based on quantum dot (QD) structures is the upcoming technology with promising advantages compared with state of the art technology. The so called quantum dot infrared photodetectors (QDIP) are proposed to compete successfully against the commonly used HgCdTe and quantum well photodetectors (QWIP) in a variety of applications. Normal incident infrared radiation can be detected in QDIP and the expected longer lifetime of photoexcited carriers leads to higher detectivity. Furthermore, lower dark current enables higher operation temperatures. These are the main reason why during the last few years many research groups have participated in the investigation of QDIP [3-6]. All these device characteristics are strongly connected with the band structure of the QD which will be discussed later on.

Photocurrent spectroscopy is an important method to analyze the properties of QDs. It enables the characterization of different parameters such as peak wavelength, linewidth, involved optical transitions and evaluation of responsivity and detectivity. Measurements at low temperatures are made to understand the mechanisms which impede the operation at room temperature.

Up to date, photocurrent measurements to analyze QD structures for infrared detection have been performed mostly by FTIR spectroscopy. In this measurement technique a Globar is used as a blackbody source. The light coming from the source is first split into two beams. One beam passes through a fixed way and one through a variable length due to a moved mirror. After collecting the beams, optical interference occurs at the sample. The measured electrical signal from the sample as function of the mirror position can be Fourier transformed into the wavelength region. The main precondition for using Fourier transformation is a linear system. For the investigation of infrared detectors this means, that the measured detector should be linear. This hypothesis could be broken by a nonlinear effect. An Auger effect was proposed by Gebhard et. al in Ref. [7] for the investigated samples measured in this paper. Using FTIR technique also vital information about carrier dynamics within the

structure is lost. Several wavelengths are simultaneously incident on the sample and different photocurrent generation mechanisms occur at the same time.

In this work monochromatic excitation was used to measure photocurrent spectra. This technique has been used before with quartz lamps for measurements in the visible and in the near infrared region below 3μm [8]. The main drawback is that this measurement technique is relatively slow compared with FTIR. Every wavelength has to be measured separately. Furthermore, due to the high absorption of light in the infrared region the optical throughput of a monochromator system is very low. The advantage of monochromatic excitation is that the signal is measured in the wavelength region and therefore no transformation is used to get the photocurrent spectra. As a result, also nonlinear effects can be measured with this technique. Another advantage is that different current mechanisms can be measured separately because only monochromatic light reaches the sample.

Two different QD structures which are described in Chapter 3 were investigated in this paper. The sample type "A" consists of InAs QDs covered by InP grown on a InGaAlAs quaternary material lattice matched to InP. Sample type "B" shows the same QD structure but with an InGaAs quantum well (QW) embedded in the quaternary material.

The main research in this work was the intraband measurement of the type A sample structures which show a wavelength peak at around 6.4μm with monochromatic excitation. Type B samples which have a peak wavelength at 12μm, were not measured in this work. Due to the very low intraband photocurrent signal observed in type A samples further investigation has to be done to maximize the optical throughput of the monochromator system to measure longer wavelength. Interband photocurrent and dark current measurements for both sample types have also been performed.

## 1.2  The Status of Research

One of the most important methods to grow QD structures is the self assembling Stranski-Krastanow (SK) growth method. A drawback is the inhomogeneous formation of the QDs. To fully control the density and/or size of QD structures, new methods are investigated as in situ electron-beam (EB) lithography [9] and atomic-force nanolithography [10]. In the latter case an electrostatic field applied between a conductive AFM tip is used to locally oxidize the surface of a sample to grow QDs on pre-determined positions. Material combinations such as InGaAs on GaAs, Ge on Si and InAs on InP have been reported. This growth mechanism gives lithographic resolution in the order of tens of nanometers depending on the applied force. Another site-control technique was reported growing InAs QDs on GaAs substrates using a combination of in situ EB lithography and self-organized molecular-beam epitaxy. A thin oxide layer is formed on a GaAs mesa structure followed by in situ lithography and $Cl_2$ gas etching writing an indentation pattern. The oxide is removed and a thin GaAs buffer is deposited on top followed by a QD-layer growth in self assembly in the SK mode. The density of the QDs in each indentation can be controlled by changing its depth. In indentations with a depth of 5-6 monolayer single QD were successfully nucleated.

InAs is a very interesting material for optical applications. Such QDs are sensitive for IR radiation covering the wavelength region between 3µm and 40µm. By combining band gap engineering and self-organized growth of QDs the MWIR absorption properties can be changed and desired energy transitions in QDIPs can be achieved. It has been shown that for embedded self-organized InAs QDs in an AlAs/GaAs superlattice structures, the optical transition energy can be tuned by changing the superlattice period and the growth conditions of the dots [11].

One of the main reasons for using QD structures for infrared detection is the possibility of using such detectors at high temperatures due to expected lower dark current and longer carrier lifetime. The main goal is to design a

QDIP operating at 77K to use liquid nitrogen for cooling instead of helium. Wang et al demonstrated in Ref. [12] reduced dark current by introducing a thin AlGaAs barrier layer between InAs QDs and GaAs. The corresponding detectivity was $2.5*10^9$ cm $Hz^{1/2}$/W at a peak wavelength of 6.5µm, which was the highest detectivity reported for QDIP at 77K in 2001. Nowadays QDIPs reach detectivities as high as $3*10^{11}$ cm $Hz^{1/2}$/W at a peak wavelength of 4.7µm [13]. However, higher detectivity at longer wavelengths is desired. Another progress concerning this topic was presented in Ref. [14] where a QDIP operating up to room temperature is reported. The dark current was lowered by using structures where the InAs QDs were coupled with GaInAs QWs with AlInAs barrier layers grown on InP. Photocurrent around 4.1 µm coming from a bound to bound transition was observed. Although the responsivity and therefore the detectivity decrease with increasing temperature this research shows the possibilities using QDIP at high temperatures.

Typical dark current blocking layers also block the photocurrent at longer wavelength. Barve et al mentioned this in Ref. [15] and proposed reducing the dark current by using resonant tunneling barriers. Quantum dot-in-a-well (DWELL) detector structures where InAs QDs are placed inside an InGaAs QW grown on GaAs were investigated. Two 2nm AlGaAs barriers allow the carrier within a certain energy band to pass through, while blocking a continuum of energies and therefore reducing the dark current over three orders of magnitudes compared with a control sample. The detectivity was $3.6*10^9$ cm $Hz^{1/2}$/W at 77K at a peak wavelength of 11µm. The authors suggest that a significant improvement in the device performance can be expected by the use of better design of the structure.

Multicolor infrared detection can offer a better target discrimination, tracking, and identification as well as temperature determination and are very useful in industry for gas leakage detection, chemical analysis, and for environmental sensing and control [16]. The detection of buried land mines [17] is an application of multicolor infrared detectors of high interest which can save human life in many regions of the world.

Two-color detectors based on HgCdTe material [18] and QWIPs [19] have been demonstrated. However, there are only few reports of the development of two-color devices based on QDIP. Ma et al. reports in Ref. [20] a voltage tunable two-color InAs/GaAs QDIP working under normal incident infrared radiation. This was achieved by the combination of a photovoltaic and a photoconductive response. The first is related to the transition of electrons from the ground state to the continuum by applying small bias leading to a photocurrent peak at 5.5 µm. The latter occurs at bias voltages above 0.7V due to tunneling of excited electrons through the tilted barrier leading to a photocurrent peak at 7.0µm.

A bias-selectable tricolor QDIP was demonstrated by Ariyawansa et al in Ref. [21]. The device consists of a so called tunneling QDIP (T-QDP) architecture based on InGaAs QDs grown on AlGaAs. Excited electrons are collected by resonant tunneling across an AlGaAs/ InGaAs/AlGaAs double barrier coupled to the QDs. Depending on the bias electrons can tunnel trough the barriers and are collected by the field leading to photocurrent peaks at 9.5µm (forward bias) and 16.9µm (reverse bias). A peak around 4.7µm occurs for positive and negative bias voltages. It is proposed that by tuning this T-QDIP structure a detector working in the 3-5 and 8-14 µm atmospheric windows can be designed which is desired for future infrared systems.

Another very complex and important research area is the space science. Observation of cold and hot objects, on earth and in space, with very different background requirements is desired. At the Air Force Research Laboratory the use of infrared detectors in satellites for surveillance and situation awareness missions is investigated [22]. Extremely uniform arrays for tracking to detect images within only one or two pixel, low power consumption due to the limited satellite power, low weight and small volume to save launch costs and extremely low detector noise are the main problems to be solved. The idea is to develop a monolithically-integrated sensor system in which each pixel has a protection, an amplification, a detection and a solid-state cooling layer using quantum dot structures among others.

Rogalski shows in Ref. [5], that for the last 25 years, infrared detector array size has been increasing at an exponential rate, following Moore´s law with the number of pixels doubling every 19 months. Figure 1.1 shows the number of pixels per array as a function of the year in which such a detector array was first used. The newest data in the graph was used from Raytheon Vision Systems which manufactured a 4kx4k focal plane array (FPA) based on HgCdTe technology. For further information refer to [23]. To the best of our knowledge no further information of future array sizes were available at the time of this work, but it is predicted that FPAs of 100 megapixels and larger will be possible [24]. Current limitations are not based on technology but on manufacturing costs. A main problem of the HgCdTe technology is the difficult in growing layers with Hg. Therefore new material systems are under investigation.
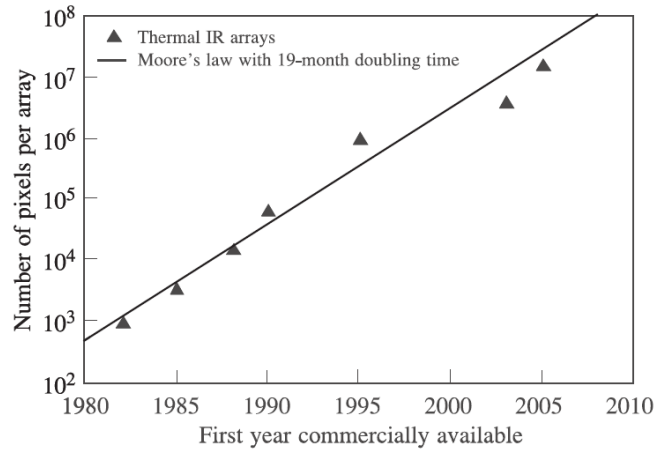


Figure 1.1: The number of pixels on an infrared array in accordance with Moore´s law with a doubling time of approximately 19 months.

Gunapala et al report in Ref. [25] a 640x512 pixels long-wavelength infrared QDIP imaging FPA. Molecular beam epitaxy (MBE) technology was used to grow multi-layer LWIR DWELL structures based on the InAs/InGaAs/GaAs material system. By controlling the dot or well sizes this hybrid device offers a good tuning of the spectral response of the photocurrent. The FPA were hybridized with a commercial readout circuit by flip-chip bonding and

successfully operated as a camera by the use of a lens system. The shown video images were taken at 60K at a frame rate of 50Hz in the 8-9μm range. This development shows that QDIP array technology offers very positive attributes for future use.

Another concept for photodetection in the infrared was done by Böberl et al at the University of Linz [8]. QDs absorbing in the infrared were filled into porous alumina membranes (PAMs) by solution processing. The formed narrow columns lead to a vertical charge carrier path between the contacts. Two different materials were investigated. 4nm PbS QDs showed photocurrent in the near infrared with cut-off wavelength of 1.25μm. By increasing the dot size and changing the compound material photocurrent up to 3μm with 6nm HgTe QDs was reported. Although the cut-off wavelengths are relatively short, the approach to infiltrate QDs into porous membranes can be extended to other nonporous membranes which can also be flexible or even elastic which enables new device applications.

In spite of the performed research until now, further investigation has to be done to improve the characteristics of the developed QDIP. Lowering the dark current and increasing the detectivity are the main topics to meet the future needs of such novel infrared devices. Phillips points out in Ref. [26], that the main reason for poor QDIP performance can generally be linked to two sources: nonoptimal band structure and nonuniformity in QD size. Additional energy levels in QDs between excited and ground state similar to the thermal temperature or where phonon scattering is permitted may decrease carrier lifetime and therefore increase dark current and reduce detectivity. One of the main reasons for the current low performance of QDIP is the QD size nonuniformity leading to a broadening of the energy levels which reduces the detector peak response.

# Chapter 2

# Theoretical Background

## 2.1 Theory of Quantum Dots

Quantum dots are 0-dimensional nanostructures embedded in a compound semiconductor which a larger bandgap leading to three-dimensional quantum confinement. Even at room temperature electrons are captured in the dot and their energies have discrete values. As a result, if an electron moves from a higher energy level to a deeper level a photon according to the energy difference is emitted. This effect is used in quantum dot lasers (for further information refer to [27]). If a photon with a certain energy is absorbed by an electron in the QD the resulting current can be measured. This can be used to design photodetectors and is discussed in this work.

As mentioned previously the electrons are confined in all three dimensions in the QD. This occurs if the size of the QD is near the de Broglie wavelength of the electrons. The potential energy of bound carriers in a QD is quantized like in atoms, whereas the states in the conduction band are referred to as bound electron states and the states in the valance band as bound hole states[1]. The typical height of QDs is between 5 and 10nm and the typical width between 20 and 50nm. A variety of different shapes of QDs like cones, square based pyramids, thick lenses and flat lenses have been grown [28]. The electrical properties of the QDs are defined by quantum effects and the physical properties depend on their size, shape, uniformity and doping. Increasing the

---

[1] This is without correspondence to the atomic like electron energy configuration.

size of the QD red shifts the emission spectrum for bound to continuum transitions. Conversely, decreasing the size shifts the spectrum to shorter wavelength. Size distribution of a QD ensemble broadens the spectrum.

QDs can be realized by photo- or electron beam - lithography (top-down) or by spontaneous formation (bottom-up). The latter can be achieved by the Stranski-Krastanow (SK) growth mode. Lithography techniques are not suitable for mass production due to the slow process. This is the reason why the SK method is the most popular technique used now.

The first epitaxial growth of quantum dot structures was made 1993 by using molecular beam epitaxy (MBE) [29] based on the SK growth mode. Nowadays such structures can also be produced by chemical vapor deposition (CVD) and metal-organic chemical vapor deposition (MOCVD) [30] also using the SK growth method. The samples measured in this work were grown by MOCVD.

Up to now, the most studied system of self-assembled QDs is the InAs/GaAs system [31-34]. But also other systems for different applications have been grown such as InAs/InGaAs, InAs/AlGaAs [35], InGaAs/AlGaAs [21], GaN/AlN [36], Ge/Si [37]. There are only a few reports of growing InAs/InP QD structures [38-41]. Such structures have been regarded as one of the most promising material systems to fabricate QDIP, although only a few results of the infrared characteristics of such structures were reported [3, 42, 43]. In this work InAs QDs grown on InP substrates are investigated.

In general QDs are very attractive candidates for many optical applications such as QD lasers because of the lower threshold current compared to QW lasers [31], light emitting diodes [44], photovoltaic devices [45] and electronic applications such as modulation doped field effect transistor (MODFET) [46], single electron transistors (SETs) [36], Memories [47] and Quantum Computing [48].

## 2.2 Motivation for using QD Structures for IR Photodetectors

The chapter is organized as follows: at the beginning a brief overview of infrared detectors in general is given, than the evolution from intrinsic detectors to QD infrared photodetectors will be pointed out. It will also be clear why there is a high interest in the investigation of QD structures for infrared detection.

| Group | Type | |
|---|---|---|
| Thermal | Thermophile, bolometers, pyroelectric | |
| Photon | Intrinsic | IV-VI    (PbS, PbSe, PbSnTe) |
| | | II-VI    (HgCdTe) |
| | | III-V    (InGaAs, InAs, InSb, InAsSb) |
| | Extrinsic (..doped with:..) | Si:Ga, Si:As, Ge:Cu, Ge:Hg |
| | Free carriers | PtSi, Pt$_2$Si, IrSi |
| | Quantum wells | GaAs/AlGaAs, InGaAS/AlGaAs, InAs/InGaAs, InAs/InAsSb |
| | Quantum dots | InAs/GaAs, InGaAs/InGaP, Ge/Si, InAs/InP |

Table 2.1: Overview of infrared detectors.

In general infrared detectors can be divided, after Rogalski [49], into two groups: thermal and photon detectors (or photodetectors). The formers are thermopile, bolometer and pyroelectric devices. Although they are very cheap and can be operated at room temperature, these detectors are sparely used due to their low detectivity at high frequencies and relatively slow response [49]. Photon detectors can be further divided into intrinsic detectors, extrinsic detectors, free carrier detectors, quantum well and quantum dot infrared detectors. Table 2.1 shows an overview of infrared detectors with just a few examples of material combinations. For each detector type different modes of operation are possible such as photoconductive and photovoltaic operation.

Further information about infrared detector technology can be found in Ref. [50].

The infrared region between 1μm and 15μm is very important for many applications. Photodetectors working at these wavelengths are very interesting for free space optical communication, toxic gas detection and image recognition. The corresponding photon energy is in the range from 1,2eV to 83meV. The first step in the evolution of these photodetectors was to use interband transition in semiconductors for infrared photodetection. Materials with a relatively small bandgap have to be investigated. By calculating the long-wavelength cutoff it can be determined the value of the largest detectable wavelength of the material.
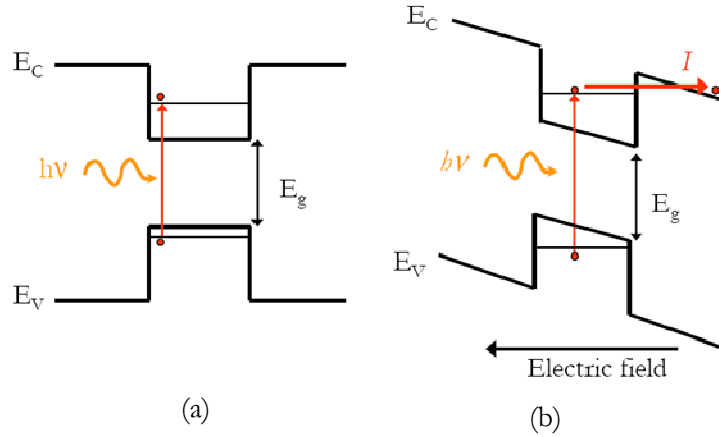


Figure 2.1: (a) Interband transition. (b) By applying an electric field it is possible to collect the electrons.

The long-wavelength cutoff for an intrinsic photoconductor [51] is given by

$$\lambda_c = \frac{1,24}{E_g}\mu m \tag{2.1}$$

where $E_g$ is in eV.

Si which has a bandgap of 1.1eV has a long-wavelength cutoff of 1μm which means, that the light with a wavelength longer than 1μm passes the sample without generating photocurrent. Figure 2.1 shows schematically the process of detecting light in an intrinsic semiconductor material. A photon with the energy $h\nu$ is absorbed by an electron which is excited from the valence band

to the conduction band. By applying an electric field the electrons can be collected as photocurrent.

Figure 2.2 shows the energy gaps of the most important semiconductor materials and alloys. There are some interesting alloys which are used for infrared photodetection beyond 1μm, some examples are: $In_xGa_{1-x}As$, $In_xAl_{1-x}As$ and InAs.

Figure 2.3 shows the absorption coefficient of various photodetector materials. Very appealing is the mercury cadmium telluride (HgCdTe) material composition which has an adjustable bandgap from 0.7 to 25μm and is the most widely used infrared detector today [18]. HgCdTe infrared detectors have been intensively developed over the last fifty years. However there are several drawbacks of these detectors. The high cost in the fabrication of HgCdTe detectors due to difficulties in growing HgCdTe materials because of the high vapor pressure of Hg and the unavailability of large size arrays are the main reasons why new material systems are desired. Furthermore these detectors are relatively slow for optical communications. As textbook for further information of HgCdTe infrared detector material Ref. [52] may be useful.

III-V semiconductor materials have been investigated to overcome the difficulties in epitaxial growth and processing of II-VI semiconductor materials [26]. Furthermore due to the absence of suitable material compositions in the desired infrared region new detection techniques have been investigated. The main problem was to find a material with a relatively small gap to detect low energy photons. The fundamental idea was to use intraband transitions (inter-subband transition, subband-subband transition) or subband–continuum transitions. In the first case a bound to bound transition takes place where the transition occurs in the conduction band by exciting an electron from one energy subband to another. This is shown in Figure 2.4. The energy of the absorbed photons is determined by the energy difference of the two subbands. In the second case the transition takes place from a subband in the conduction band to the continuum (bound to continuum transition). In the latter case the absorption is broader because there are a lot of possible energy states in the continuum. Therefore photons within a larger energy range are detected. To
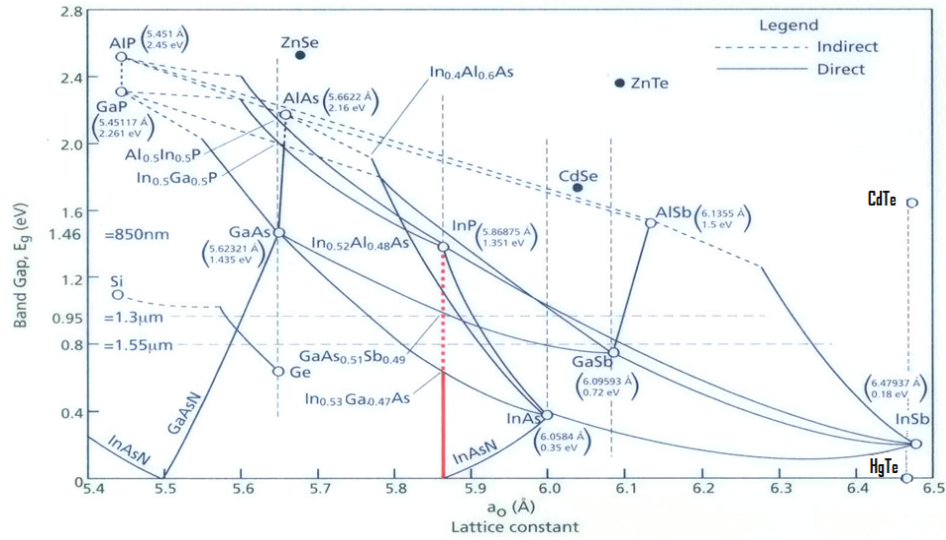
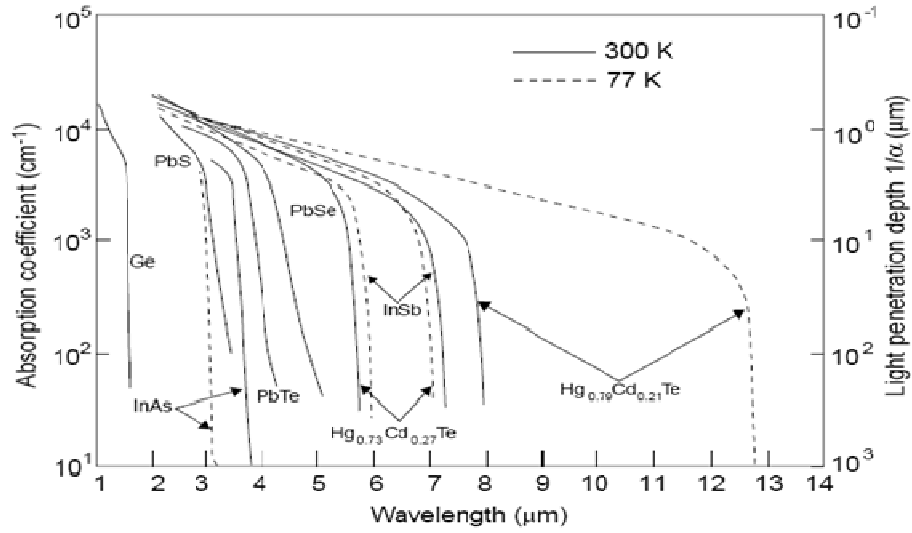Figure 2.2: Energy gap in dependence of lattice parameters for several semiconductors.



Figure 2.3: Absorption coefficient for various photodetector materials in the spectral range between 1 and 14μm at 77K and 300K [49].

design a very narrowband and wavelength selectable detector bound to bound transition should be used.

Energy subbands can be achieved in semiconductor materials by confining carriers in one direction. In a quantum well (QW) structure where energy levels are discrete in the growth direction such an intraband transition can be achieved. QWs are formed by sandwiching a material between two layers of a material with a larger bandgap. This had led to the development of Quantum Well Infrared Photodetectors (QWIP) which are widely studied today, for more information refer to [6, 53-55].
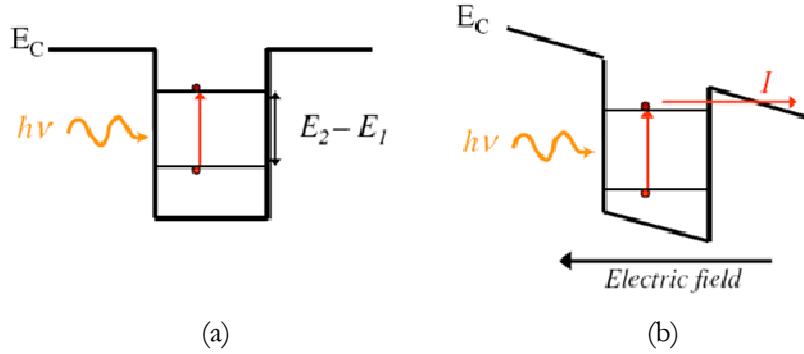


Figure 2.4: (a) Intraband transition. (b) By applying an electrical field it is possible to collect the electrons.

QWIPs are very attractive candidates to compete with HgCdTe detectors because of their lower costs in fabrication and the availability for producing large size arrays. The main drawback of QWIPs is that the intraband transitions are not allowed for light incoming parallel to the growth direction (normal incident light). As a result special optical systems have to be used to couple in the infrared radiation. The solution to this problem was to use QD structures where the electrons are confined in three dimensions and normal incident light is detectable.

## 2.3 Quantum Dot Infrared Photodetectors

QDIPs are unipolar devices, using electrons for charge transport. QDs are particularly attractive candidates for intraband infrared detection because of their sensitivity to normal incident light due to the three-dimensional confinement of carriers. The first QDIP characterization was done in 1997 at the Princeton University [56] and since then there has been a lot of research in this area although until now there are no commercial QDIP available.

It is possible to use QDIPs without the use of diffraction gratings to convert vertical incident light into in-plane incident light which is necessary in QWIPs. QDIPs provide multi-wavelength detection by tuning the energy spacing between bound energy levels varying size, shape, and material composition of QDs [2].

Compared to higher-dimensional structures the discrete energy spectrum of QDs leads to a drastic slow-down of the electron relaxation of excited states, this has been predicted as the so-called phonon bottleneck effect [57] where the intraband energy spacing is larger than the LO phonon energy.

A longer excited electron lifetime in QDs leads to a higher photoconductive gain[2] than QWIPs because photoexcited carriers are probably collected before relaxing to the ground state of the QD [2]. This should lead into higher detectivity and higher operation temperatures [31]. Due to the lower dark current a higher signal-to-noise ratio is expected than in QWIPs [49]. Better noise properties of QDIPs can be explained by the reduced unwanted electron scattering mechanisms due to the discrete energetic structure in QDs [11]. Also the unipolar character of the intraband QDIPs avoids generation-recombination noise.

One of the main disadvantages of QDIPs is the large linewidth of a QD ensemble due to size distribution in the Stranski -Krastranow growth mode [49]. This means that the optical absorption coefficient is reduced because it is inversely proportional to the linewidth.

---

[2] Photoconductive gain = Ratio between lifetime and transition time of the carrier through the detector.

The optical absorption coefficient can be expressed as a function of the linewidth σ of the transition [58, p.374]

$$\alpha \sim \frac{3.5 \times 10^5}{\sigma[meV]} \, cm^{-1}. \tag{2.2}$$

Thus, even through each QD has a sharp transition energy, the absorption of a self assembled grown QD-ensemble shows an inhomogeneous broadening due to the Gaussian size distribution of the QDs. Vertical coupling of stacked quantum dot layers can reduce the inhomogeneous linewidth but increases the dark current of the device, since carriers can tunnel through adjacent dot layers more easily [49].



Figure 2.5: Schematic of a vertical InAs/InP QDIP with multiple QD layers as is measured in this paper.

There are two different kinds of device structures. A vertical QDIP is shown in Figure 2.5. This is the type of samples which is measured and presented in this work. Usually there are 10 or more QD layers stacked between highly doped contact layers. The photocurrent is collected between these two

layers which serve as top and ground contacts. The QDs can be doped or undoped.

The second type of detector structure is a lateral QDIP. The transport occurs between two top contacts in a high-mobility channel. This is comparable to a field effect transistor (FET). Lateral QDIPs seems to have lower dark current and higher operating temperatures but are difficult to integrate into FPAs bonded to silicon read out circuits. For this reason more investigation is focused in vertical QDIPs [49].

# Chapter 3

# Sample Characterization

## 3.1  Sample Growth and Preparation

All samples were grown in the Laboratório de Semicondutores (LabSem) at the Catolic University of Rio de Janeiro (PUC Rio) in Brazil by metalorganic vapour phase epitaxy (MOVPE). A detailed description of the growth process can be found in Ref. [59] and is, for the better understanding of the measurements, also listed in the following.

Two types of QDIP structures were grown by MOVPE on semi-insulating InP (100) substrates at 100mbars, as shown in the schemes of Figure 3.1 . For both types of sample a 150nm thick InP buffer layer is deposited at 630 °C on the substrate followed by a 500nm thick n-doped InGaAs layer lattice matched to InP. For sample A, on top of the InGaAs layer, the quaternary material InGaAlAs with thickness of 109nm is grown with 16% Al content and lattice matched to the substrate. The InAs quantum dots are then deposited for 5.5s at 520 °C. The dots are annealed in an arsine atmosphere for 12s. They are covered by a 13nm thick InP layer while the temperature is ramped up to 600°C. These three different layers are repeated ten times. A 60nm layer of the quaternary material is then grown, and, finally, a 250nm n-doped InGaAs contact layer is deposited. In the case of sample B on top of the quaternary material lattice matched to the substrate with thickness of 99nm and Al content of 16%, the periodic structure consisting of a 10 nm InGaAs lattice matched quantum well followed by a thin barrier of 3nm of the same quaternary material, on top of which InAs QDs are nucleated

and covered by an InP layer, is deposited under the same conditions as for sample A. For this structure the number of periods is also 10. A 60nm layer of the quaternary material is then grown, and, finally, a 250nm n-doped InGaAs contact layer is deposited. All ternary and quaternary layers are grown at 600°C. Figure 3.1 also shows the profile of the conduction band of the investigated samples. The doping level at the contact layers is $1.0\mathrm{x}10^{18}\mathrm{cm}^{-3}$.

The composition of the quaternary material was chosen so as to maximize the dot density. In order to keep the density and the QD size unchanged after the growth of ten layers, a thick InGaAlAs barrier was chosen [59].

**Sample Type A**



**Sample Type B**
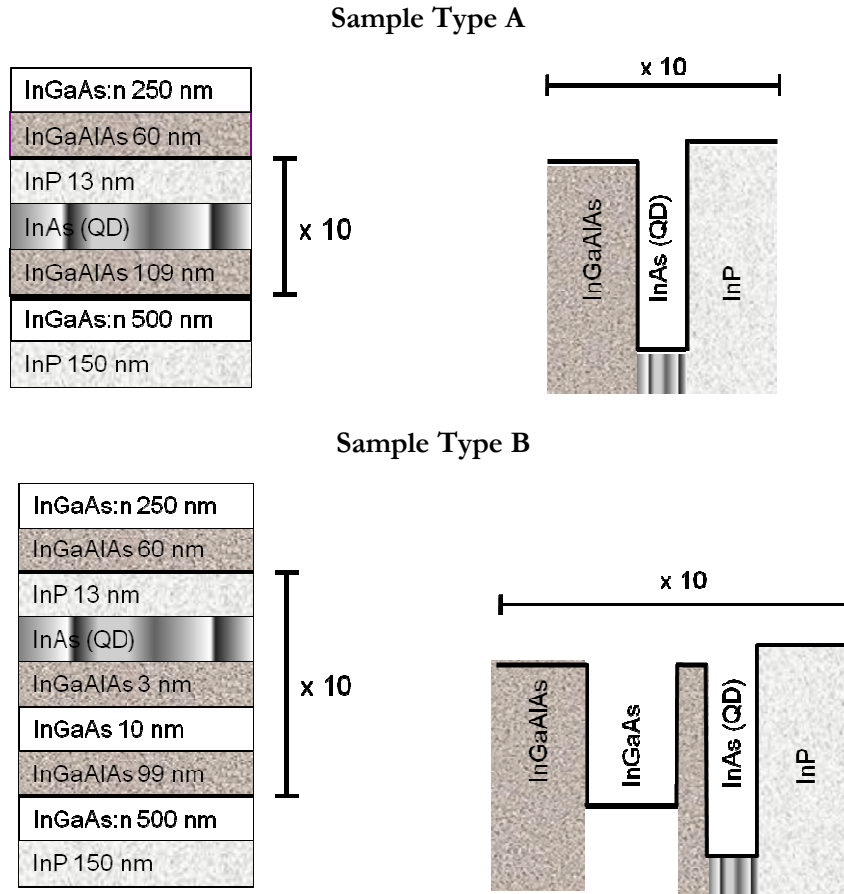


Figure 3.1: Scheme of the structures of samples type A and B (left) and conduction band profile along the growth direction (right).

The grown samples were processed by photolithography to get several detectors on each sample. Afterwards the samples were mounted on a chip carrier and contacts to the chip carrier leads were performed to enable an easy measurement. Each chip carrier includes two different samples. One sample consits of several detectors each with an optical window of 120x120μm which one can see in Figure 3.2. The detectors are all connected by the bottom contact of the sample which serves as ground connection. Furthermore all detectors have a top gold contact connected to the chip carrier from where the signals are measured. For each sample there are three to four detectors connected to the chip carrier.
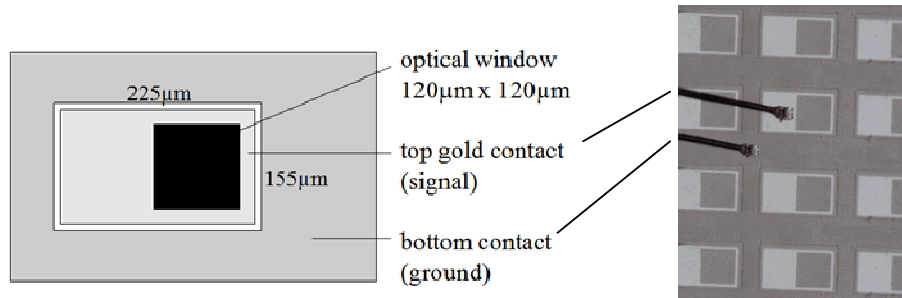


Figure 3.2: Schematic of one detector and photo taken through light microscope.

## 3.2  Description of the Samples

Atomic force microscopy (AFM) images and scanning transmission electron microscopy (STEM) images were made to determine the height, density, base diameter and shape of the quantum dots.

According to the atomic force microscopy (AFM) images of control samples where the QDs were left uncapped, the dot density is $1.5 \times 10^{10}$ QDs/cm$^2$ and the height is 9nm on the average for both samples. An AFM image of one QD layer is shown in Figure 3.3.

Figure 3.4 shows a low resolution bright field STEM image o the sample structure B. The left image shows the substrate, the n-doped InGaAs bottom contact layer, the 10 QW – QD layers and the n-doped InGaAs top contact layer. The right image shows a higher resolution of the multilayers. The image shows

cylindrical symmetry QDs, lens shaped, with a base diameter of approximately 50 nm. The average dot height of 9nm was confirmed with STEM measurement.
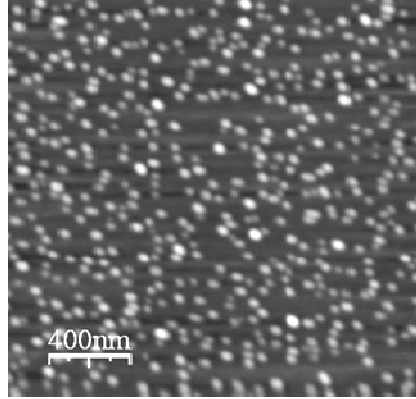


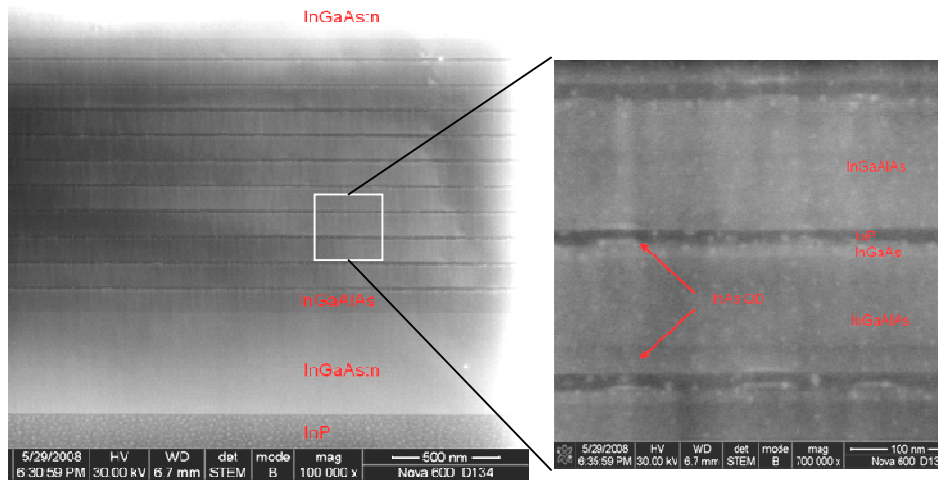Figure 3.3: AFM Image of one quantum dot layer.



Figure 3.4: Low resolution bright field STEM images showing the sample type B structure.

The size of the QD is inhomogeneously broadened due to the self assembled growth in the SK-growth mode. Figure 3.5 shows the distribution of the 9nm dot height with a deviation of 1.5nm. The variation in dot size leads to a broadening of the measured photocurrent spectrum.
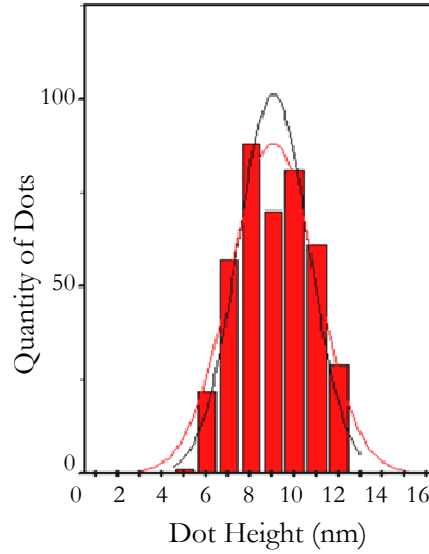


Figure 3.5: Distribution of 9 nm dot height with a deviation of 1.5nm.

Three samples for each sample type with different dot doping levels were grown: A nominally undoped sample with one electron per dot, one with two electrons per dot and one with four electrons per dot. The doping material was silicon.

All samples consist of 10 QD layers with bottom (ground) and top contacts. A schematic of the sample can be seen in Figure 2.5. The detectivity of the investigated QDIPs is estimated to be around $10^9$cm $Hz^{1/2}$/W at temperatures below 70K, comparable to a typical QWIP in the same wavelength range.

On page 78 a detailed description with all layer dimensions of the different samples can be seen. In the observation column the deposition times for each layer is given. The samples are n-i-n structures, meaning highly doped contact layers with an intrinsic area between them (see also Figure 5.13).

## 3.3  Type A Band Structure Calculation

The sample type A has been modeled by Souza et.al in Ref. [59] using a three-dimensional effective mass approximation for the conduction band to identify the optical transition leading to the measured intraband photocurrent in this work. The physical parameters of the materials were used from Ref [60]. The Schrödinger equation was solved by expanding in terms of eigenfunctions of a large infinite barrier cylinder of the length L and radii R which can be seen in Figure 3.6.
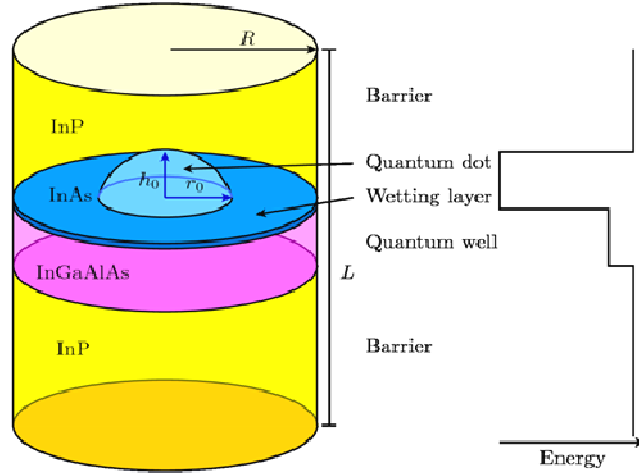


Figure 3.6: Use of the eigenfunctions of a large infinite barrier cylinder (left) to solve the Schrödinger equation and conduction band profile (right).
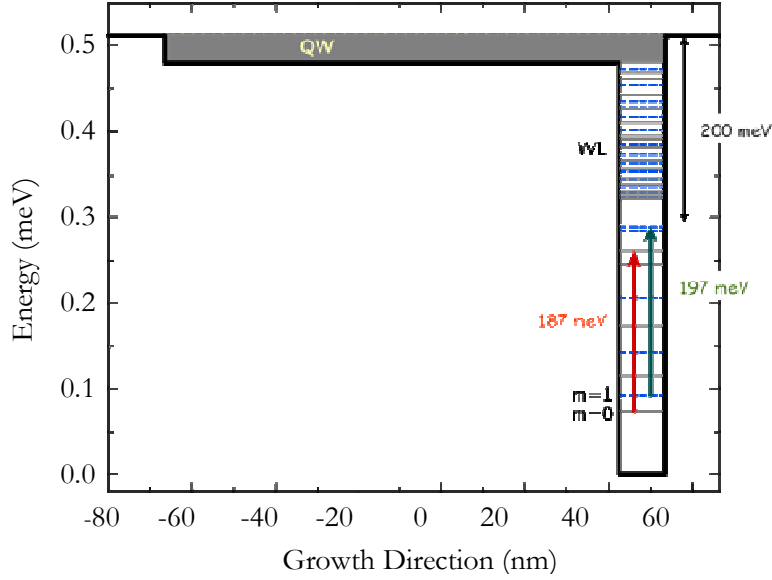
Figure 3.7: Calculated energy levels in the conduction band for quantum numbers m=0 (solid line) and m=1(dashed line) for sample type A versus growth direction [7].

The results of the effective mass calculation are shown in Figure 3.7 for the quantum numbers m=0 and m=1 and discussed in Ref. [7]. The optical transitions for which the oscillator strength is largest are shown by arrows. Also the QW from the InGaAlAs material and the energy levels from the InAs wetting layer (WL) are shown. The results of the calculations indicate that the strongest absorption for normal incident light occurs for energies around 187meV (m=0) and 197meV (m=1), respectively. The excited electrons are still deep in the QD after the optical transition and a carrier transport mechanism is needed to generate photocurrent. This will be discussed later on.
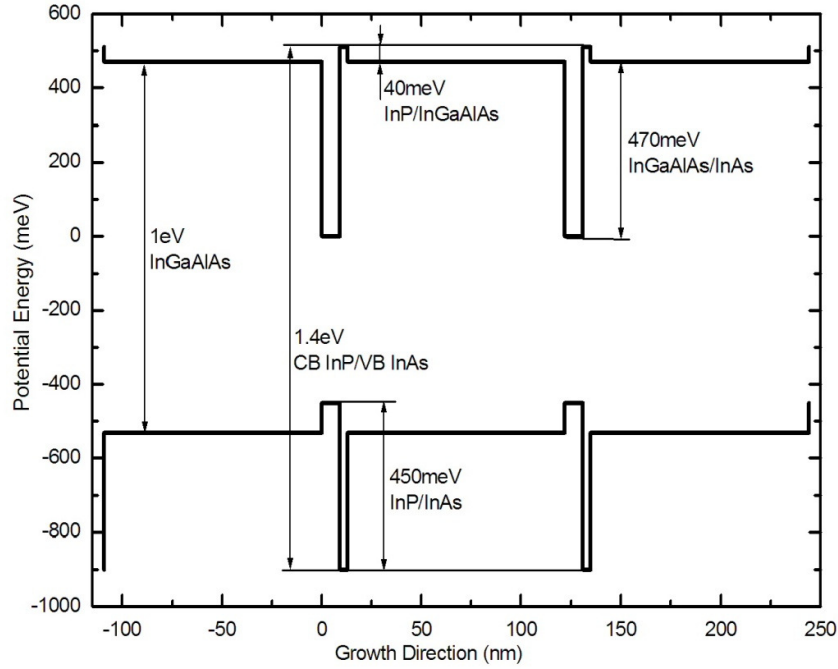
Figure 3.8: Energy levels in dependence of growth direction for the conduction band (CB) and the valence band (VB) of type A samples.

The band alignment of conduction and valence band is shown in Figure 3.8. The potential depth of the QD is 470meV. This figure is important to analyze the photocurrent measurements discussed later on in chapter 5.

## 3.4  FTIR measured Photocurrent of Type A

The FTIR measurements of the samples were done at the Photonics Institute and Center for Micro and Nanostructures at the Technical University of Vienna and further information can be obtained from Ref. [7]. As can be seen in Figure 3.7 the final state of the optical transition is about 200mV from the continuum. This means that a carrier transport mechanism is required to generate photocurrent. A tunneling mechanism can be ruled out because of the relatively thick barriers. Probably an Auger process is taking place where an electron from a

higher level relaxes to the ground state and transfers its energy to an electron on a deeper state. This electron has now enough energy to escape the QD to the continuum and photocurrent is generated by the intrinsic field. A schematic representation of this effect is shown in Figure 3.9 (b) and the FTIR measured intraband photocurrent in Figure 3.10.
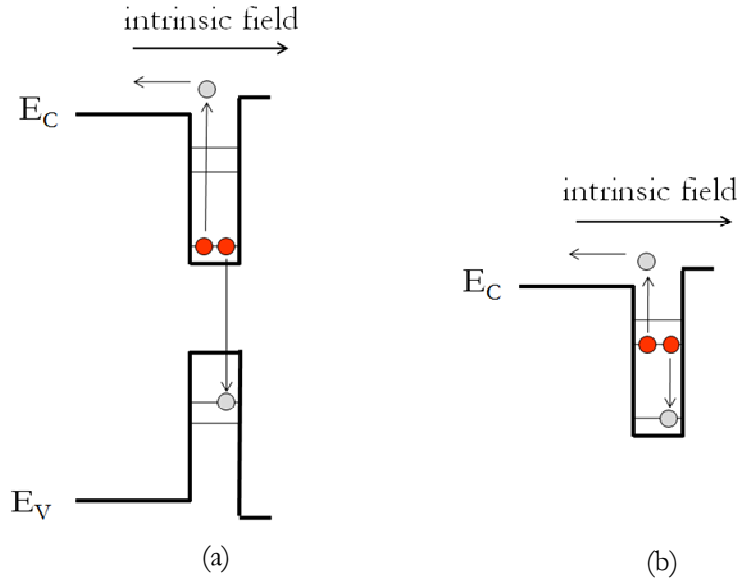


Figure 3.9: Interband (a) and Intraband (b) Auger process.

The observed narrow peak in Figure 3.10 at 190meV of the undoped sample comes from the intraband absorption of carriers from residual doping and carriers transported from the contact layers to the dots. The carriers will populate first the ground state of the larger dots and only a few dots with smaller size distribution will participate in the photocurrent. The photocurrent peak is more than 10 times smaller and three times narrower than that for the doped sample. It can be observed that increasing the doping broadens the spectrum. This occurs because more QDs with a larger size distribution contribute to the photocurrent. Furthermore in some dots there are more than 2 (or 4) doped electrons leading to absorption also between other energy levels. It should be pointed out, that these

measurements were done by FTIR using a broadband light source. That means that different optical transitions, due to the polychromatic radiation, take place at the same time. To ensure that only one optical process occurs, monochromatic excitation can be used as investigated in this work and described in Chapter 4.
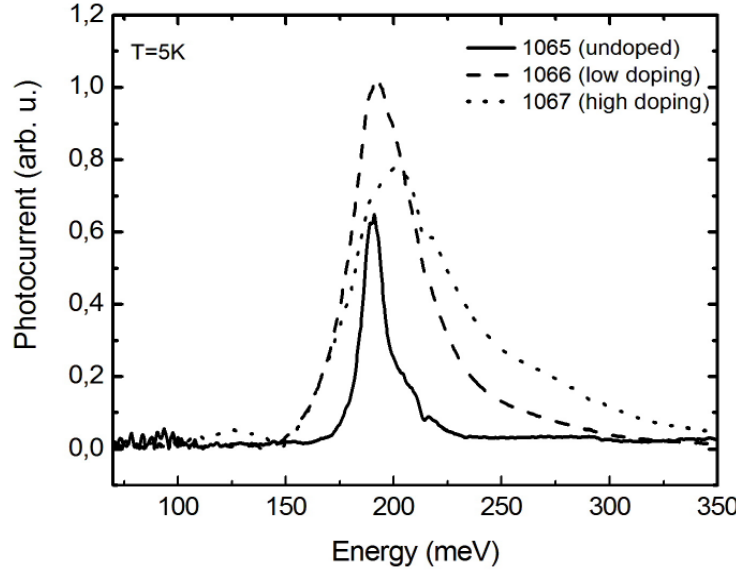


Figure 3.10: FTIR measured intraband photocurrent of all three samples from type A at 5K and without bias.

Interband photocurrent from excited electrons from the valence band to the ground state in the undoped sample can be seen in Figure 3.11. This photocurrent is generated due to an interband Auger effect as can be seen Figure 3.9 (a). An electron from the conduction band recombines with a photogenerated hole in the valence band and transfers its energy to the photoexcited electron.

Photocurrent at energies below 800meV is not temperature dependent and originates from electrons excited to the lowest energy level in the conduction band. However, photocurrent between 800 and 1000meV, corresponding to electrons excited to higher levels, depends on the temperature. This can be explained that due to thermal excitation electrons can be excited to these higher

energy levels. The strong photocurrent peak above 1000meV originates from the InGaAlAs barrier layers.

Interband photocurrent measurements (here not shown) for the doped samples of type A show a different behavior. The peak below 800meV is comparable with the undoped sample. However, photocurrent between 800 and 1000meV increase with decreasing temperature.

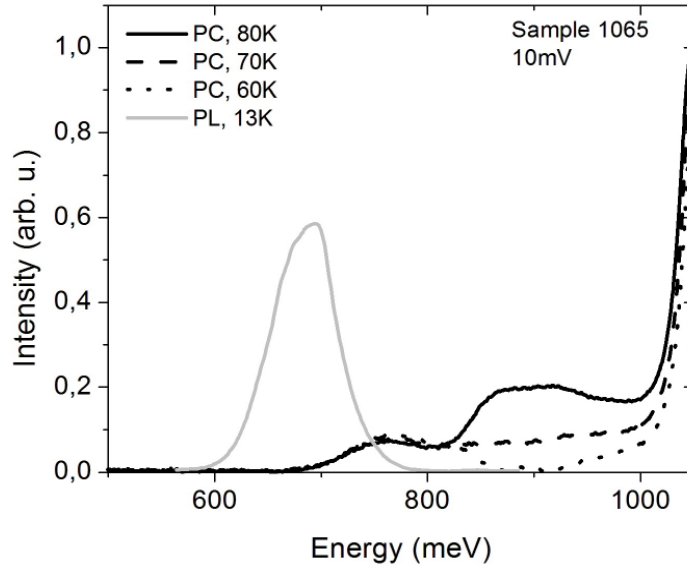There are several processes and phenomena which are not fully understand and further investigations have to be done.



Figure 3.11: FTIR measured interband photocurrent of the undoped sample (type A) at different temperatures biased with 10mV and photoluminescence (PL) at 13K.

Photoluminescence at 13K for the undoped sample can be seen in Figure 3.11. The luminescence spectrum around 700meV originates from the recombination of electron and hole ground states of the QDs.

## 3.5  Motivation of Sample Type B

Until now, QDs have been grown in a variety of different shapes and sizes, although it is very difficult to tune the optical transition energies in the QDs by variation of growth parameters. However, changing the QD environment influence also the transition energy scheme [11]. Therefore, samples of type B, as shown in Figure 3.1, have been grown. In this hybrid sample, InGaAs QWs are coupled to the QD layers, forming a QD-QW periodic lattice. This offers a way to design transition energies by varying the QW width or the QW composition. Changing the QD size would be much more complicated and cannot be varied by much.

Until now no band structure calculations have been done for this type of samples. FTIR measurements showed a narrow peak at 12.1μm and another weak one was detected at 5.9μm. This indicates that by simply changing the thickness of the QW and of the InGaAlAs layers on top of it, selective wavelength detection (until 12.5μm) can be achieved.

# Chapter 4

# Apparatus

## 4.1 Interband Measurement Setup

The basic setup to measure interband photocurrent is shown in Figure 4.1. The used devices and a picture of the system setup can be seen in the section Experimental Setup on page 79.

A closed cycle cryostat was used to perform measurements at temperatures down to 15K. The monochromator was controlled by a specially adapted Lab-View control panel running on a PC. A plain halogen lamp from OSRAM was used as radiation source. The spectral curve can be seen in Figure 4.2 and will be discussed later on.

As can be seen in Figure 4.1 the emitted light from the halogen lamp passes through the monochromator where the light is spectrally decomposed by a grating and narrow-band-filtering by a slit aperture.

Only the selected wavelength and its harmonics (multiples of the selected wavelengths) can pass the monochromator. To identify the very small photocurrent signal in the noisy environment coming from background radiation the lock-in technique is used. Therefore an optical chopper is placed at the output of the monochromator. A chopper frequency of 160Hz was chosen to avoid multiples of 60Hz of the Brazilian power system in order to get rid of disturbing modulations.

The monochromatic light beam gets first collimated and then focused, both with two lenses, on the sample. The sample is connected to a low noise transimpedance preamplifier which amplifies the photocurrent coming from the

QD layers. The preamplifier also provides the bias voltage. The preamplifier output signal is then amplified by the lock-in. The lock-in amplifier measures and amplifies only the frequency component that corresponds to the chopper frequency. The analog output signal is digitalized by an A/D converter and handed over to the PC through an USB interface.
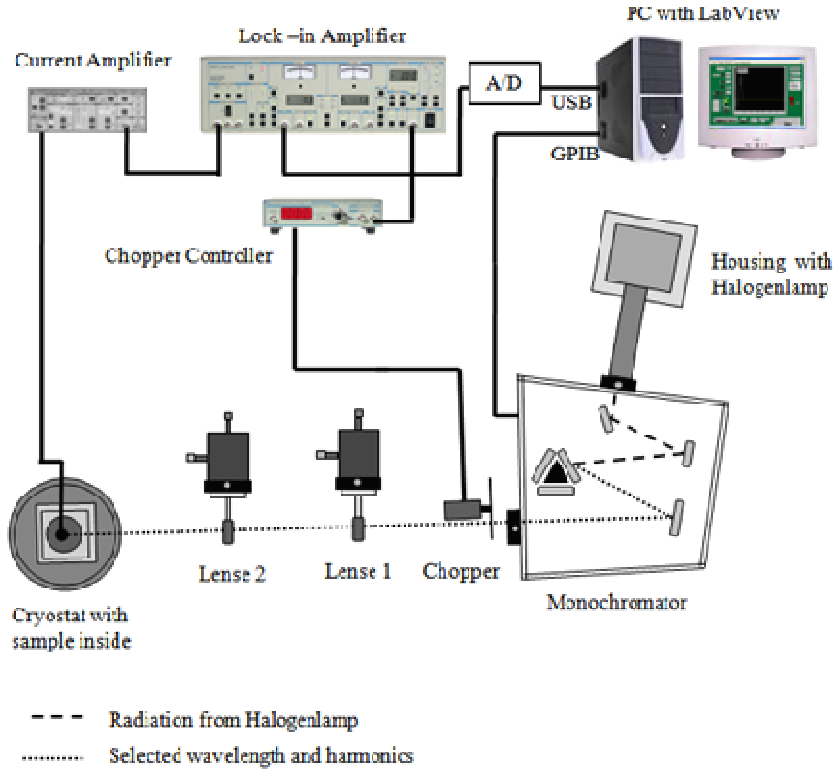


Figure 4.1: Schematic illustration of the interband measurement setup.

The spectral resolution and range of the measurement can be adjusted by the Lab-View program. Furthermore the space between two wavelengths can be changed. The interband measurements were done with a wavelength step of one or ten nanometers. The monochromator gets controlled via GPIB. The points of the measurement are logged in a text file. The curve of the photocurrent response is instantaneously shown on the Lab-View panel.
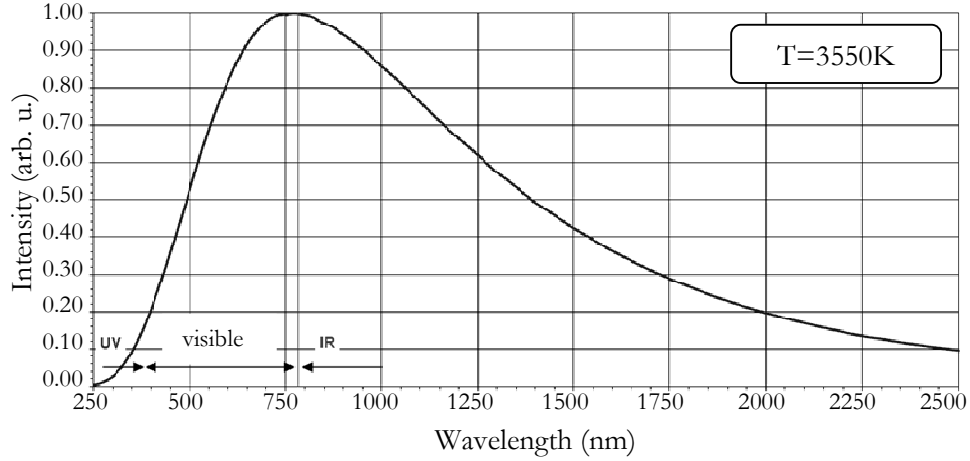
Figure 4.2: Spectral intensity of the used lamp OSRAM HLX64655 (source: OSRAM).

The light source used in this setup is a standard halogen lamp OSRAM HLX64655 with the spectral intensity shown in Figure 4.2. To estimate the peak wavelength of the lamp, Wien´s displacement law $(\lambda_{peak}T = 2897.77\mu mK)$ can be used.

$$\lambda_{peak} = \frac{2897.77\mu mK}{3550K} = 816nm \qquad (4.1)$$

Hence the maximum temperature is known as 3550K the peak wavelength is 816nm. Halogen lamps have a high output power in the visible light and the very near infrared region. Beyond 2µm the radiation is very weak and becomes zero rapidly. As a result this lamp has no emission in the MWIR and can therefore only be used for the interband measurements.

The results of the interband measurements and discussions are shown in Chapter 5.

## 4.2  Intraband Measurement Setup

The intraband measurement setup shown in Figure 4.3 is similar to that for interband with some modification for the light source and the used lenses. The most important adjustment in this setup is the lamp. A standard halogen lamp emits light between 250nm and 2.5μm which is equal to energy among 4.96eV and 0.496eV. There is no radiation in the MWIR and LWIR because the quartz lamp bulb of a halogen lamp cuts off the infrared radiation beyond 2.5μm.
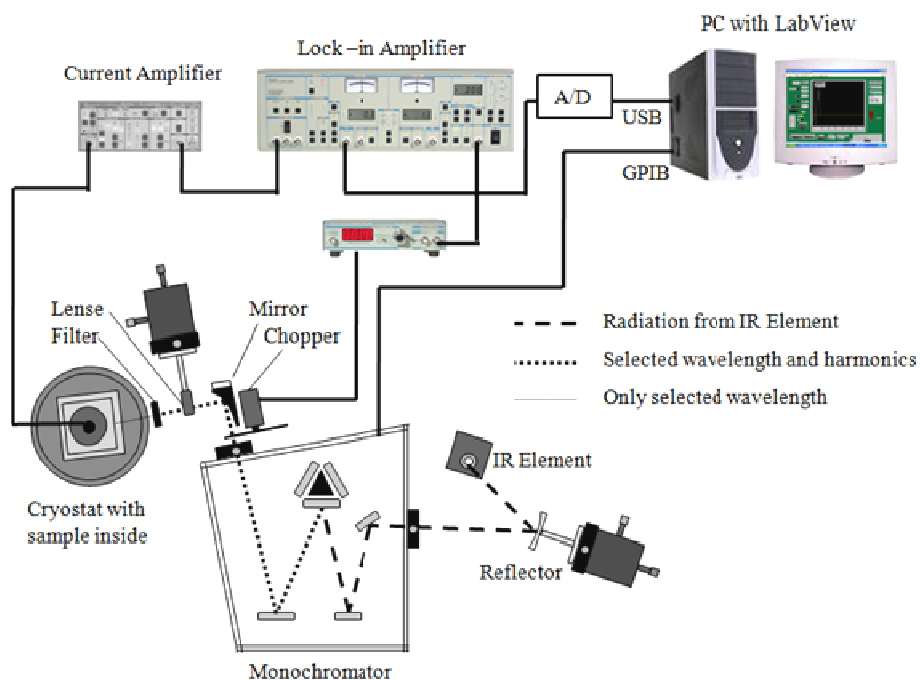


Figure 4.3: Schematic illustration of the intraband measurement setup.

An appropriate light source must be used to cover the mid infrared range. The most commonly used sources for FTIR spectroscopy are the so called Globar lamps acting as a blackbody source. The integral spectral power in a standard FTIR spectrometer is about 12 W. A slightly stronger source (LOT Oriel LSB151) with 30 W was used in the measurements to increase the signal-to-noise ratio.

The infrared lamp which can be seen in Figure 4.4 consists of a ceramic core with a platinum heater imbedded in a ceramic coating around it. The ceramic is of the same metal oxides as that of Nernst glowers and therefore has the same optical and physical characteristics. The radiation area is about 3.2mm wide by 13mm long. It has reasonably high output in the 1–5µm range. Above ~7µm the irradiance which can be seen in Figure 4.5 is similar to that of a full radiator with the same 1500K temperature [61].



Figure 4.4: The LSB151 30W infrared element from LOT Oriel.

A drawback of the used infrared source is the very low average lifetime. Only 600h of duration powered with 20W and 400h powered with 30W are expected. To ensure the maximum lifetime the radiometric power supply (Model 68931) from Newport Oriel was used. To minimize stress on the lamp this power supply gradually ramps the current up and down. The power supply of the infrared lamp was operated in current mode in the range between 6.8-8.2A.

The optical components in the setup of chapter 4.1 consisting out of glass must be exchanged by ZnSe in order to enable measurements in the mid infrared range. Standard glass and lenses show a high absorption in the infrared range above 3µm. ZnSe transmits light between 0.5µm and 20µm [62]. Figure 4.6 shows the transmission profile of ZnSe. A drawback of this material is the lower transmittance compared with glasses made of quartz. As can be seen, 30% of the signal is lost due to the higher reflection index.
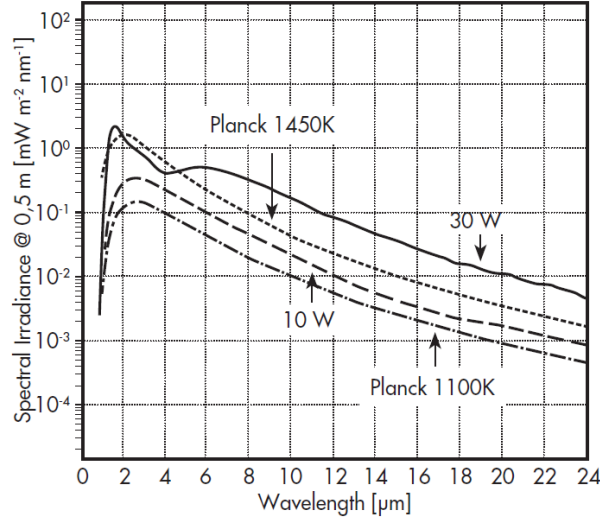
Figure 4.5: Spectral irradiance dependence of the wavelength of the used 30W IR source compared with the black body spectrum at temperatures 1100K and 1450K.

The diameter of the cryostat window was not conform with standard size ZnSe windows. So it had to be adapted. Regarding the toxicity of ZnSe this must be done carefully. The handling of the window was also very difficult due to the small diameter of the window.

A new grating with a line density of 150 lines/mm and a primary spectral range of 2.5 and 12μm was mounted in the monochromator. The grating was calibrated using harmonics wavelength from a standard Laser pointer which emits at 532nm.

A concave $AlMgF_2$ reflector was used to couple the light into the monochromator. The reflector was placed in such a way that an image of the infrared source appeared with a magnification of two at the entrance slit of the monochromator. [63]. At the output of the monochromator the infrared beam is collected by a parabolic mirror and then focused by a ZnSe lens with a focal length of f=50mm. To cut off lower wavelength components coming from harmonics, an InAs filter with cut-off wavelength around 3.5μm was used. The filter cuts the unwanted harmonic frequency components produced by the monochromator

grating. Especially the interband component which would appear at multiples of its wavelength can be eliminated.
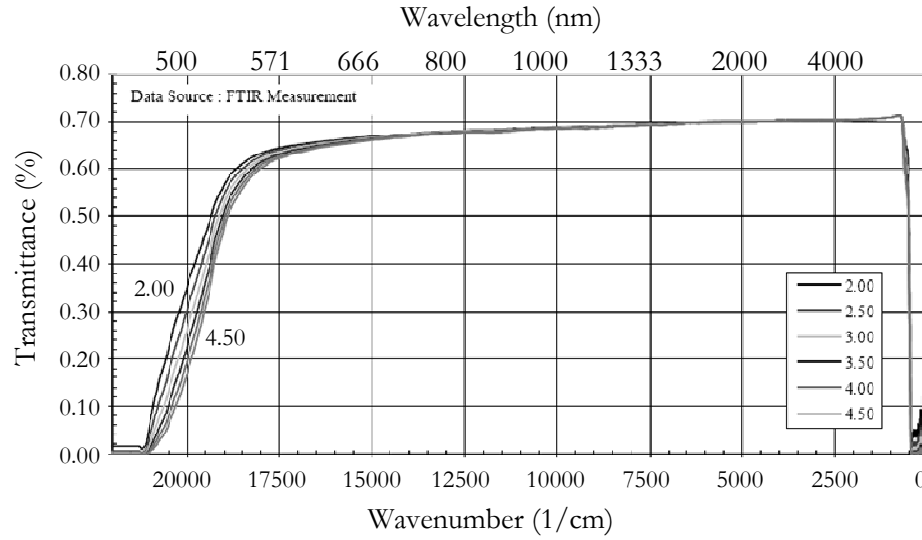


Figure 4.6: Calculated transmission profiles of ZnSe at 293K for substrate thickness between 2.0 and 4.5mm [62].

# Chapter 5

# Experimental Results

## 5.1  Dark Current and Activation Energy

Dark current ($I_C$) measurements were performed using an HP 4145B semiconductor parameter analyzer. The curves which can be seen in Figure 5.1 were measured at different temperature between 300K and 15K without illumination by applying an electric field and detecting the corresponding current. The first row shows the samples without doping, the second with low doping and the third with high doping. On the left side the results for type A samples (only QD) and on the right side for type B samples (QD and QW) can be seen. With a optical window of 120μm x 120μm a dark current of $10^{-9}$A corresponds to a dark current density of $7\times10^{-6}$A/cm$^2$.

At 300K $I_C$ is symmetric and increases with increasing temperature due to the lower thermal energy at deep temperatures. As doping increases, $I_C$ increases rapidly with bias at low temperatures. In the graph for Sample 1067 one can see, that $I_C$ at 300K and 15K at -2V bias differs only by one decade. This can be explained by the higher carrier concentration in this sample. However, Sample 1070 which is also highly doped but consists of QDs and QWs shows lower $I_C$ at low temperatures and same bias. Free electrons are captured in the QWs which serve as a trap lowering the $I_C$. Lower $I_C$ indicates higher possible operation temperatures.

For the undoped samples the curves show a symmetric behavior for both bias directions. The characteristics become asymmetric as doping increases. Reverse
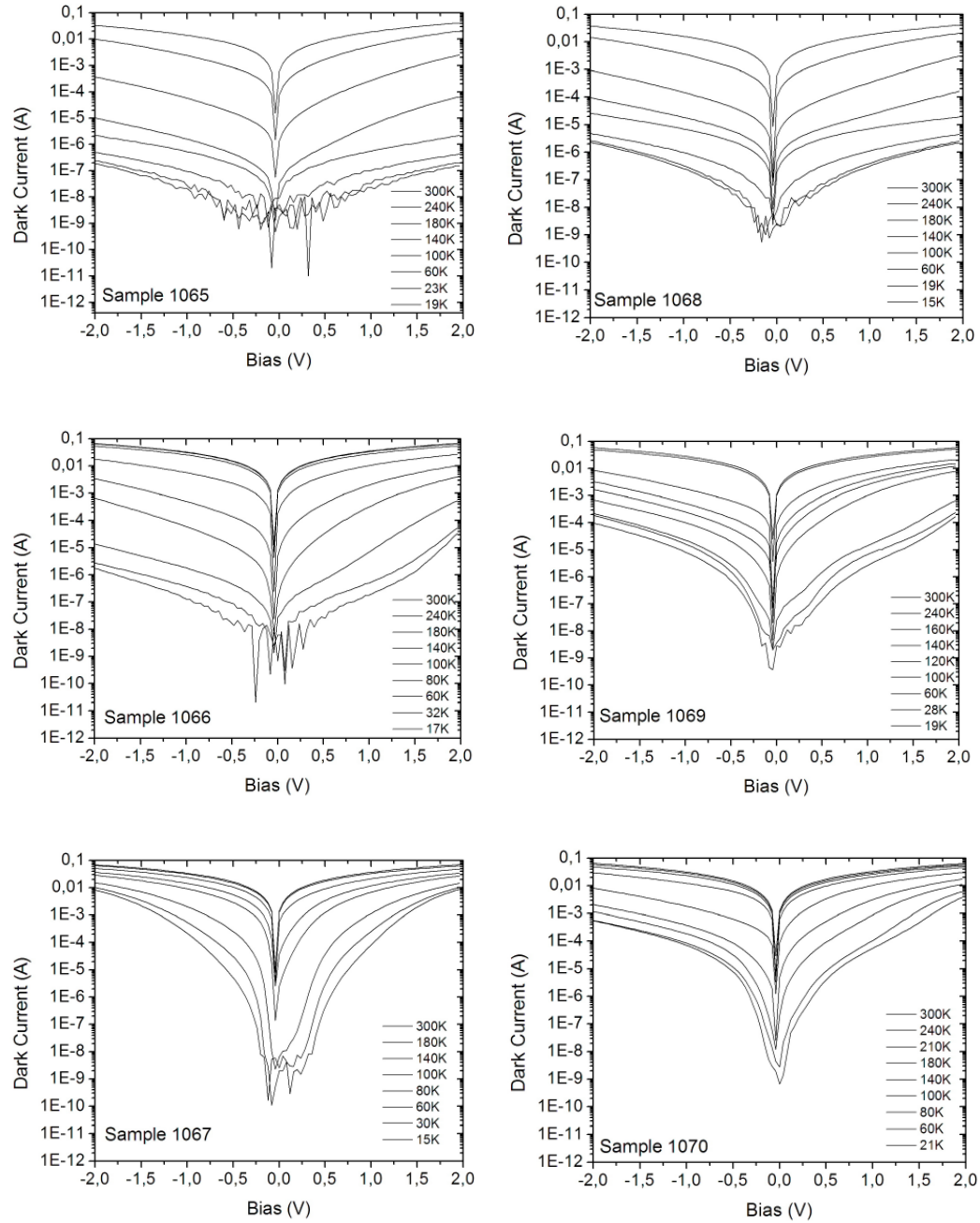
Figure 5.1: Dark current dependence on bias for type A samples (left side) and type B samples (right side).

biased, $I_C$ is lower than forward biased. This can be observed especially at low temperatures and in the doped samples. As the dark current is lower, photocurrent can be measured with a better signal-to-noise ratio.

Various interpretations of DC curves and activation energies in QDIPs have been suggested [4, 64-65]. In this paper the activation energy was calculated using the simplified Arrhenius equation for the dark current [66]
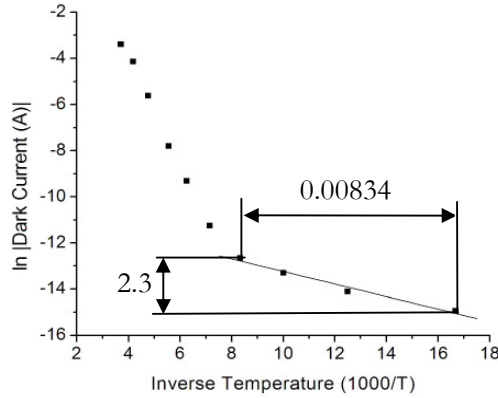
$$I = I_0 e^{-\frac{E_a}{kT}} \tag{5.1}$$

where $E_a$ is the activation energy, $I_0$ is a constant and T is the absolute temperature. Using equation 5.1 for two different temperatures the constant $I_0$ can be eliminated and $E_a$ can be calculated.

$$\frac{I_1}{I_2} = e^{-(\frac{E_a}{kT_1} - \frac{E_a}{kT_2})} \tag{5.2}$$

$$E_a = -\frac{\ln(I_1) - \ln(I_2)}{\frac{1}{T_1} - \frac{1}{T_2}} k \qquad \text{(Joule)} \tag{5.3}$$

$$E_a = -\frac{\ln(I_1) - \ln(I_2)}{\frac{1}{T_1} - \frac{1}{T_2}} * \frac{k}{e} = -\frac{\ln(I_1) - \ln(I_2)}{\frac{1}{T_1} - \frac{1}{T_2}} * 0.08625 \qquad \text{(meV)} \tag{5.4}$$



$$E = \frac{2.3}{0.00834 \frac{1}{K}} * \frac{1.38 * 10^{-23} \frac{J}{K}}{1.6 * 10^{-19} \frac{J}{eV}} * 1000 \frac{meV}{eV} =$$

$$= \frac{2.3}{0.00834} * 0.08625 meV = 23.7 meV$$

Figure 5.2: Arrhenius plot with the calculation of the activation energy in the range between 60K and 120K.

In the Arrhenius plot from Figure 5.2 it is possible to get the activation energy from the gradient of the dark current function. Thus the gradient multiplied by 0.08625 gives the energy in values of meV.

Figure 5.3 shows the dark current curves versus inverse temperature for type A samples in the temperature range between 300K and 60 K. The left side shows negative bias and the right side positive bias measurements. From this curves the activation energy can be calculated as described on the previous page. Note that the dark current scale is logarithmic. The so extracted activation energies for samples from type A can be seen in Figure 5.4. Three temperature regions between 300K and 15K have been observed for all samples. Two temperature regions are shown in the graph: on the left side for high temperatures (starting with 300K) and on the right side for lower temperatures (above 60K). For temperatures below 60K the activation energies are very small and listed in Table 5.1 for 2V negative bias. The main focus of this work was the investigation of type A samples, therefore the activation energies of type B are not discussed at this point.

| Sample | Temperature Range | Activation Energy |
|--------|-------------------|-------------------|
| 1065 | 60K – 19K | 2.3meV |
| 1066 | 50K – 17K | 1.5meV |
| 1067 | 40K – 15K | 0.5meV |

Table 5.1: Activation energies for deep temperatures reverse biased with 2V.

From Figure 5.4 it can be seen, that the activation energy decreases by increasing doping in the higher temperature range (left side). This has already been shown in Ref. [65]. At these temperatures the carriers originate from the QDs. Due to the higher carrier concentration in the doped samples the activation energy is smaller since also higher energy levels are occupied. As the temperature increases the thermal energy increases. As a result at lower temperatures no more carriers can be liberated from the dot only through thermal energy. This occurs between 120 and 140K for the undoped sample and between 160 and 140K for

the doped samples. At these temperatures it is expected, that the dark current originates only from the heavily doped contact layers.

An abrupt change of the energy at zero bias for samples 1065 and 1066 in both temperature regions can be observed. It shows that at zero and at negative bias activation energy is higher than at positive bias. This abrupt change of the activation energy can be explained by the asymmetric band profile of the QD structure. Compared with the dark current curves in Figure 5.1 it can be seen, that the dark current at negative bias is smaller than at positive bias for the same temperature. This is also an indication for the asymmetric band structure.

The activation energy for sample 1067 shows a different behavior. This sample is highly doped and therefore scattering mechanisms occur which are not fully understood until now. Also interband photocurrent measurements show a different behavior, as it will be seen later on. The activation energy is very small for the high temperature region as expected for the highly doped samples.

The relatively low activation energy for very low temperatures (below 60K) observed in all samples (see Table 5.1) can be explained by a random fluctuation in the effective bandedge [58, p.101]. This is caused by randomly placed impurities in the heavily doped InGaAs contact layers and fluctuation on the composition of the quaternary matrix material.
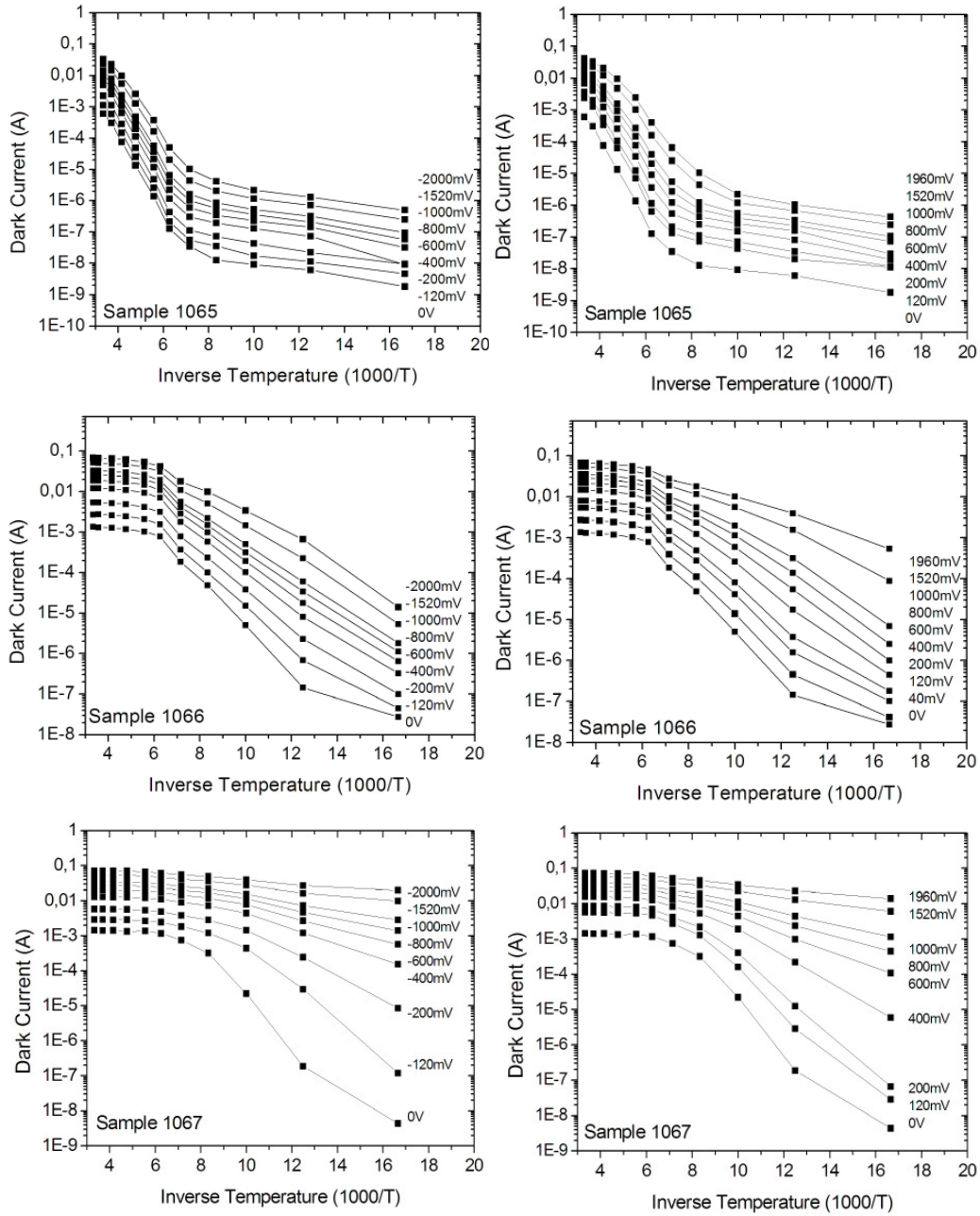
Figure 5.3: Dark current versus inverse temperature in the range between 300 K and 60K for the type A samples. On the left side results for negative bias and on the right side for positive bias are shown.
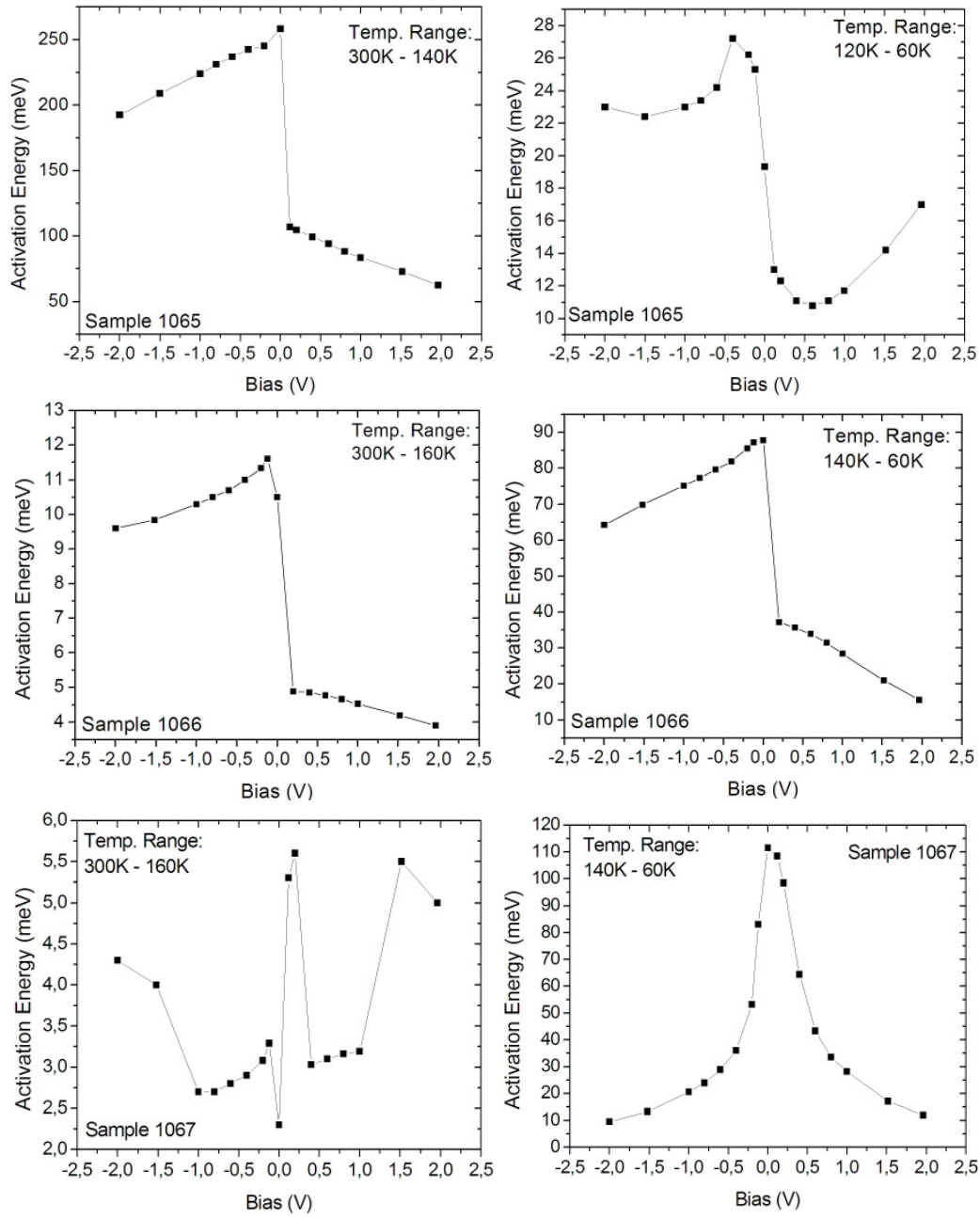
Figure 5.4: Activation energy for type A samples dependence on bias for two temperature ranges are shown, left side for high temperature and right side for lower temperature.

## 5.2 Interband Photocurrent Measurement

To analyze the measured photocurrent curves it is important to know the response of the measurement setup. For this reason the system response was measured with the Indium Arsenide Detectors J12TE2 from Judson Technologies and can be seen in Figure 5.5.
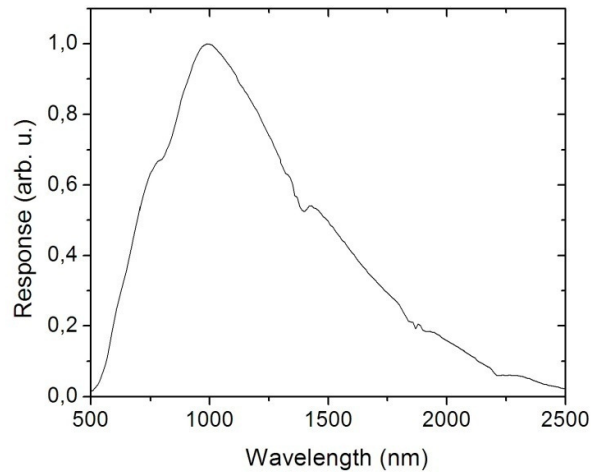


Figure 5.5: System response of the interband measurement setup (corrected by the source).

The system response contains all the influence of the optical system. Compared with the spectral density of the used Halogen Lamp from Figure 4.2 it can be concluded, that the peak wavelength of the system response moves to longer wavelengths. This can be explained by the used grating which has its blaze wavelength at 1000nm.

All photocurrent curves are shown, if not mentioned, as measured without correction by the source. The measured interband photocurrent of all samples is in the range of nanoampere. To compare different measurements the curves are often normalized.

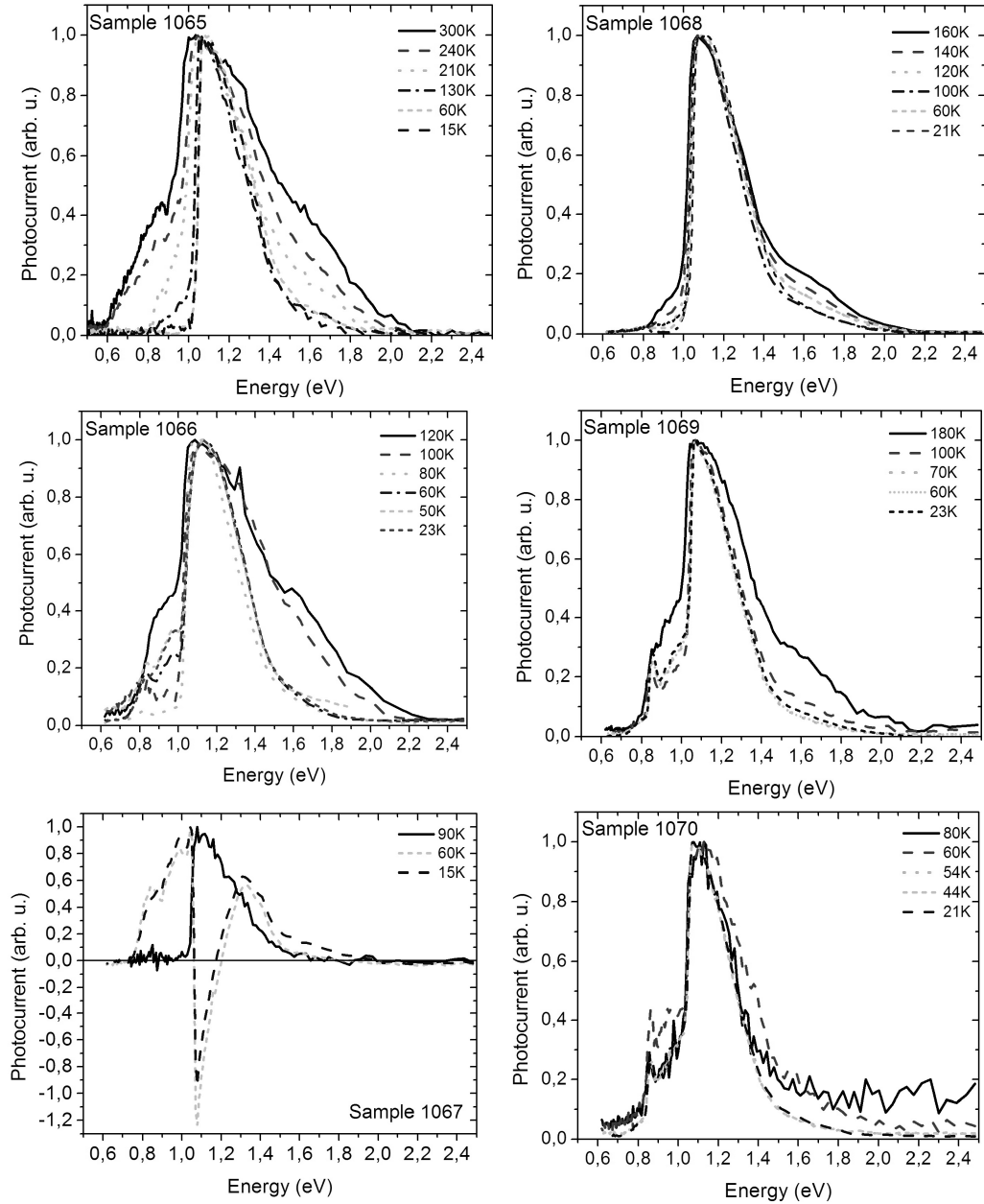## 5.2.1 Photocurrent Dependence on Temperature



Figure 5.6: Interband photocurrent dependence on energy for all samples, measured at different temperatures and without bias.

For the interpretation of the interband photocurrent measurements shown in Figure 5.6 the band profile from Figure 3.8 serves. The main photocurrent peak with cut-off energy around 1eV corresponds to the InGaAlAs quaternary material. The cut-off energy as a function of temperature and of bias is shown in Figure 5.7. As was expected, 3D characteristics can be observed from the barrier material.
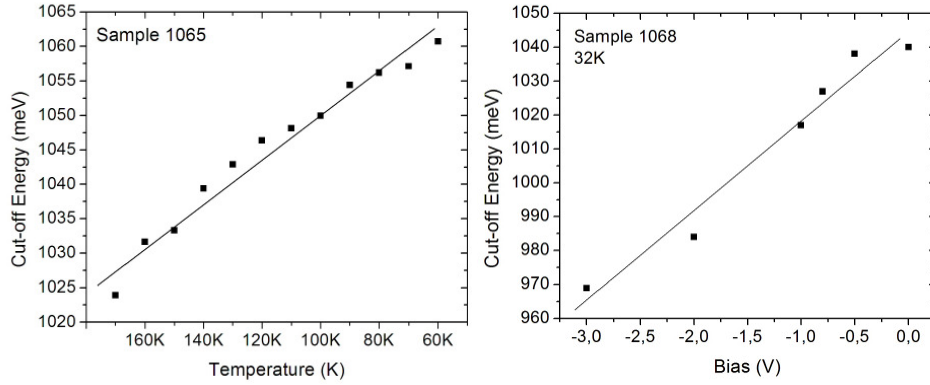


Figure 5.7: Quaternary material cut-off energy dependence on temperature for sample 1065 (left) and dependence on reverse bias for sample 1068 (right).

In Sample 1065 the photocurrent at energies around 800meV is strongly temperature dependent and probably only one optical transition can be observed. In the low doped sample (1066) photocurrent cannot be measured above 120K, due to the higher dark current in the structure. Two different optical transitions occur in this sample. Photocurrent around 800meV is generated by electrons excited to lower lying conduction energy states. Electrons excited to higher energy levels lead to a photocurrent around 900meV which is strongly temperature dependent. These results correspond to the FTIR measurements discussed in Chapter 3. The electrons excited to higher energy levels depend on thermal energy to escape from the QD and are therefore temperature dependent. Electrons promoted to the lowest energy levels rely on another escape mechanism due to the temperature independence. An Auger process was suggested by Gebhard et al. in Ref. [7] and these results give further evidence.

As the dark current is even higher in the highly doped sample (1067) photocurrent can be measured only at low temperatures, below around 100K. At 90K photocurrent is only carried by electrons excited into the quaternary material, no current from the QD can be seen. Between 80K and 70K a change in the spectral phase of the photocurrent occurs. This phenomenon can be seen also at lower temperatures. At energies between 750 and 1000meV the photocurrent is generated by excited electrons from the ground and a higher lying state in the QD. At 1000meV an abrupt change of the photocurrent occurs. At this photon energy the excited electrons in the quaternary material are swept away by an intrinsic field in the opposite direction. At higher energies the current changes to its previous direction. The processes occurring in this sample and leading to a phase change are not yet understood. Later in this chapter the bias behavior of this sample will be analyzed and further discussed.

The highest temperature where photocurrent can be measured for sample 1068 is at 160K. As observed before, this is due to the higher dark current. Further decreasing of the temperature decreases also the photocurrent between 800 and 1000meV coming from the QD. Applying reverse bias (see Figure 5.9 for definition), photoexcited electrons in the conduction band of the QD can be swept away by the electrical field. Therefore photocurrent also generated in the dot can be measured at low temperatures and is shown in Figure 5.8.
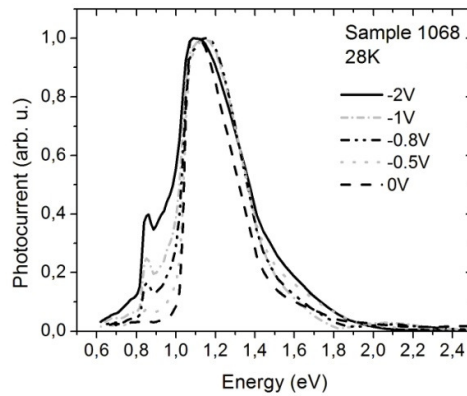


Figure 5.8: Interband photocurrent dependence on bias for sample 1068 at 28K.

Sample 1069 and 1070 show the same behavior of photocurrent respons. A peak at 850meV insensitive to temperature can be observed. Photocurrent between 900 and 1000meV is dependent on temperature. Compared with sample 1065 and 1066 this peak is relatively strong even at low temperatures. It can also be seen, that in sample 1069 photocurrent can be measured at higher temperature compared with 1066. It is believed, that the same carrier mechanism take place as described for the sample of type A.

### 5.2.2  Photocurrent Dependence on Bias

Photocurrent measurements with different applied bias were performed. Due to the different definition of bias in the literature Figure 5.9 shows how bias is applied in this work. Positive bias means that on the top contact of the sample a positive voltage is applied, for negative bias a negative voltage is applied. To further investigate the spectral change of the photocurrent in sample 1067, type A samples were measured under small bias. The bias response of sample 1068 was shown in Figure 5.8. In sample 1069 and 1070 no further information can be extracted by applying bias and is therefore not shown in this manuscript.
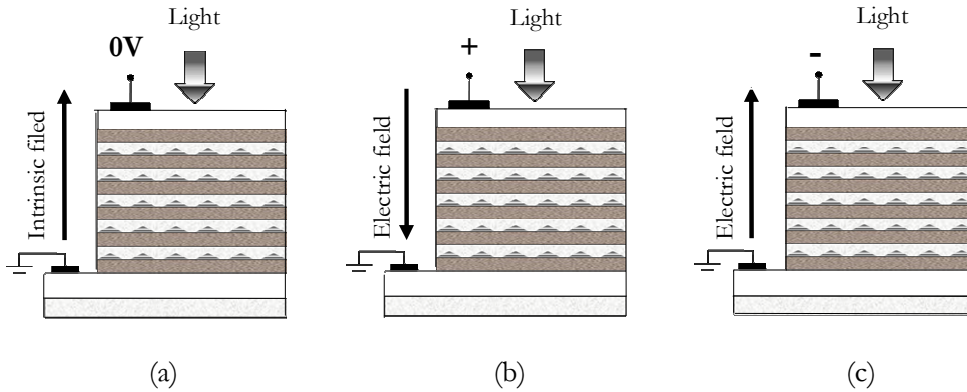


Figure 5.9: Direction of the electric field (a) without bias, (b) forward bias and (c) reverse bias.

Figure 5.9 (a) shows the intrinsic field in the stacked QD structure which leads to a photocurrent also without applied bias. This field can be explained by the geometric shape of the QDs. Perpendicular to the growth direction the structure of the QDs is asymmetric leading to this effect.

A comparison of dark current and photocurrent for sample 1066 is shown in Figure 5.10. The photocurrent was measured under polychromatic illumination by placing the monochromator grating at zero position such as all wavelengths can go through the system. As one can see, the smallest value of the photocurrent is at positive bias (therefore the intrinsic field is negative) and at negative bias for the dark current. Without applied electric field the two currents are in the opposite direction. This behavior is the same for sample 1065 and 1067.
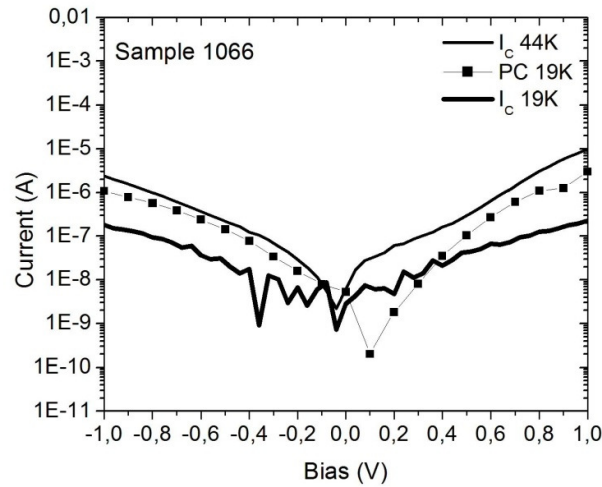


Figure 5.10: Interband photocurrent (PC) with polychromatic illumination and dark current ($I_C$) as a function of bias voltage at low temperatures for sample 1066.

The investigation of the spectral phase dependence of the photocurrent is shown in Figure 5.11. To get a higher resolution in the lower energy range the grating of the monochromator was exchanged. A grating working more efficiently at longer wavelengths was used. The legend of the bias value is in the same order as the photocurrent curves (from up to down). This remains valid also for the details shown. As one can see for sample 1065 the photocurrent originating from

the quaternary material changes the direction at a bias around 640mV. This occurs for the dot photocurrent (detail) between 300 and 400mV. The phase change occurs at smaller voltages in the low doped sample. If there are more carriers in the structure, it is easier to manipulate them by an electric field. In the highly doped sample the spectral change of the phase can be observed without electrical field which was already mentioned. Until now, we have no explanation what occurs in this sample. Further investigation has to be done.

It has to be pointed out, that no interband photocurrent could be measured in the highly doped sample using FTIR spectroscopy. No external bias could be applied. The explanation for this is still unknown. The high carrier concentration coming from the doping could lead to high noise which is not compatible with FTIR spectroscopy.
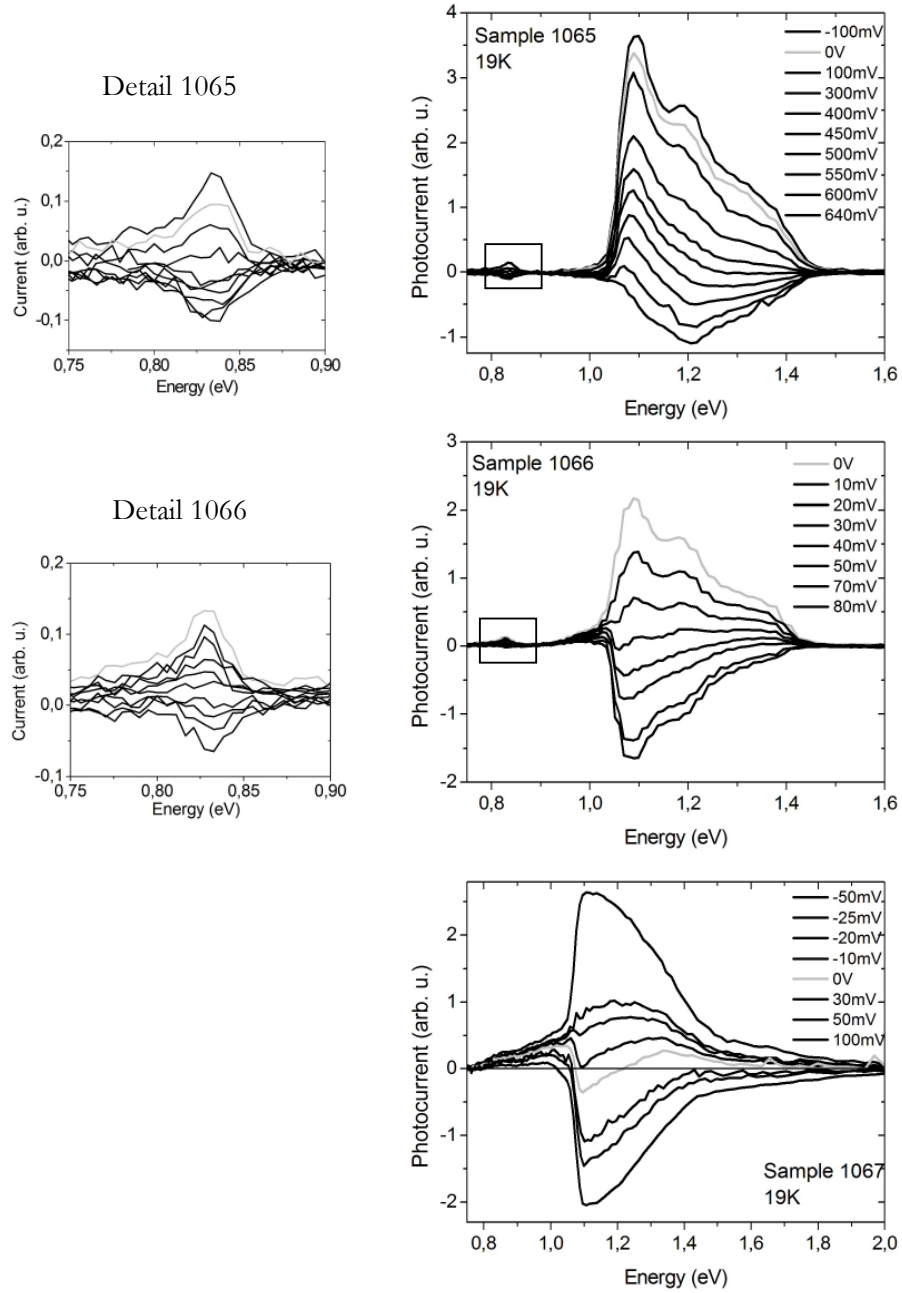
Figure 5.11: Bias dependence of interband photocurrent for type A samples. Photocurrent originating from the QD is shown in the detail.

## 5.3 Intraband Photocurrent Measurement

The main part of this work was the measurement of the intraband photocurrent. A detailed explanation of the measurement system setup can be seen on page 40. As mentioned previously the system response has to be measured to analyze the intraband photocurrent curves.
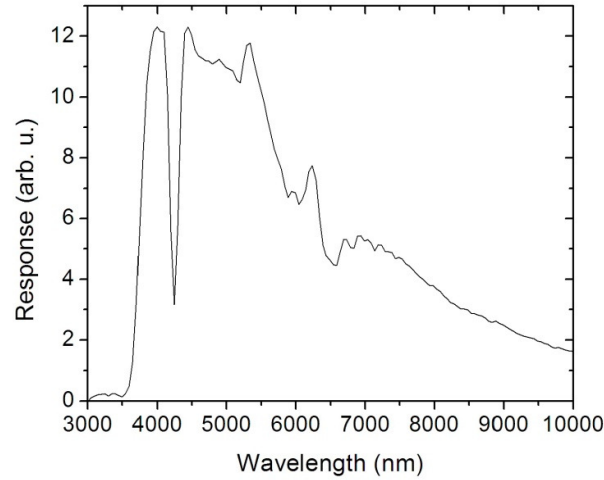


Figure 5.12: System response of the intraband measurement setup.

The system response of the intraband measurement setup can be seen in Figure 5.12. The curve was measured with a MCT detector J15D16 and corrected by the detector response.

An InAs filter with a cut-off energy of 355meV at room temperature was used. This cut-off energy corresponds to a wavelength of 3.5µm which can be seen very clearly in Figure 5.12. Furthermore the system response shows the absorption of $CO_2$ which occurs at a wavelength of 4.26µm. The lower response at higher wavelengths is related to water absorption in the air which takes place even by using a dehumidifier in the laboratory. The used grating is blazed at 4µm with a primary wavelength region between 2.5µm and 12µm.

Figure 5.13 shows a schematic potential profile of the n-i-n structure. The bottom contact is on the left side and the top contact and on the right side. Due to

the heavy doping of the contact layers the conduction band energy ($E_C$) lies below the Fermi energy ($E_F$). As the dots are undoped, the bandedge is above the $E_F$. If the dots are doped, the conduction band of the stacked QD layers sinks down depending on the doping concentration. In this case the QD energy levels are located below the $E_F$. As was shown previously in Figure 5.9, the intrinsic field points from the bottom contact to the top contact. If no external field is applied, the photoexcited electrons are collected at the bottom contact.
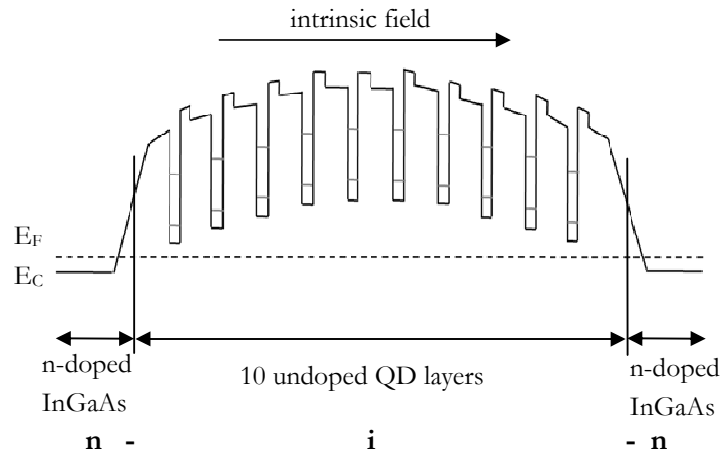


Figure 5.13: Schematic potential profile of the undoped QD structure

**Sample 1066**

The low doped sample shows a very clear intraband photocurrent. Photocurrent measured at 17K with negative bias of 1V can be seen in Figure 5.14. The peak wavelength is at 6.4μm corresponding to an energy of 195meV. Intraband photocurrent at the peak wavelength in dependence on bias can be seen in Figure 5.15. The measured peak current at 2V bias is 1.65nA. The lowest value of 0.2 pA is measured at a bias of 300mV.
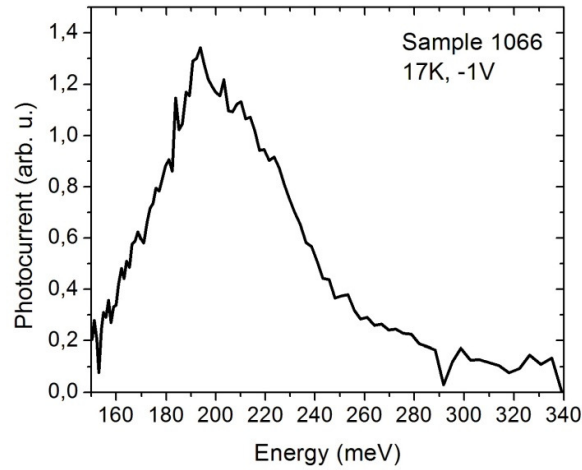
Figure 5.14: Intraband photocurrent at 17K reverse biased with1V (corrected by the source).

Photocurrent measured with better wavelength resolution is shown in Figure 5.16. Even at lower bias (-10mV) the photocurrent can be measured very clearly. Measurements with different bias were performed. Figure 5.17 shows forward biased and Figure 5.18 reverse biased photocurrent. The direction of the photocurrent changes when the intrinsic field is compensated (at around 350mV). The photocurrent can be measured with a higher signal-to-noise ratio at negative voltages compared with positive bias. This can also be seen in Figure 5.15. At positive bias the intrinsic field has to be canceled out before a positive electric field can appear. Therefore a higher voltage is needed to generate the same photocurrent as for negative bias.

Without bias the measured signal is very noisy but there is still a photocurrent observable. Figure 5.19 shows the photocurrent without bias measured at a temperature of 19K. Temperature dependence can be seen in Figure 5.20. The sample is reverse biased with 1V. The photocurrent decreases with increasing temperature. A signal was detectable up to 70K.

Compared with the FTIR measurements from Figure 3.10 it can be seen that these measurements show a lightly broader spectrum. This cannot be explained until now; further measurements have to be done to compare more different samples with FTIR results.
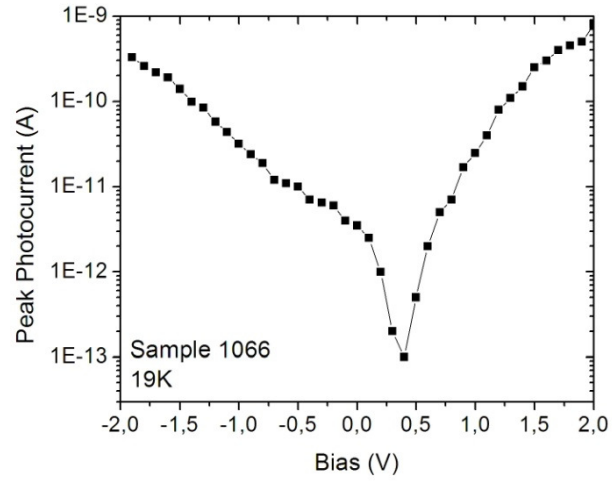
Figure 5.15: Intraband peak photocurrent dependence on bias for sample 1066 at 19K.
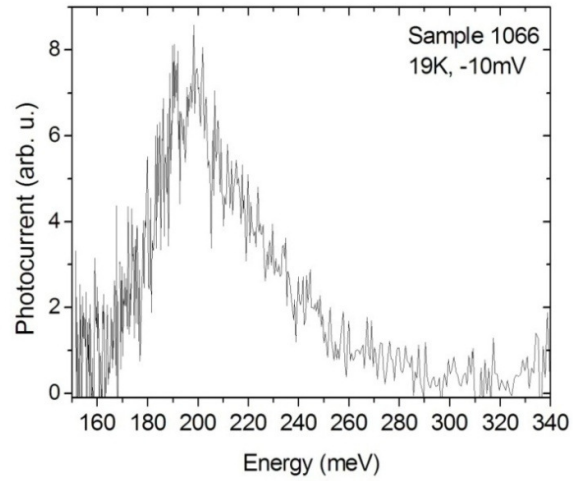


Figure 5.16: Intraband photocurrent at 19K reverse biased with 10mV (corrected by the source).

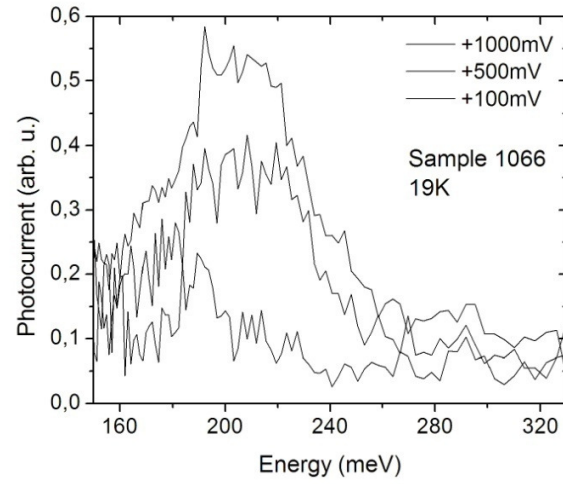Figure 5.17: Photocurrent dependence on forward bias (corrected by the source). The direction of the current is inverse to that at negative bias.
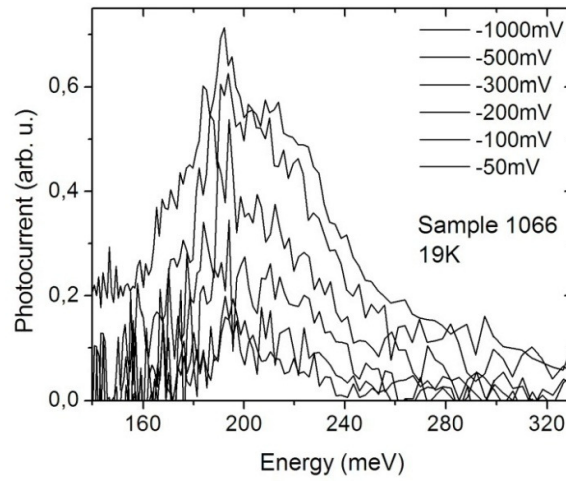


Figure 5.18: Photocurrent dependence on reversed bias (corrected by the source).
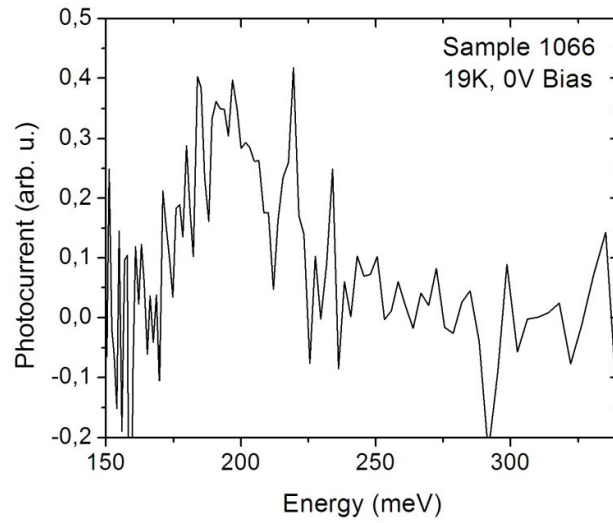
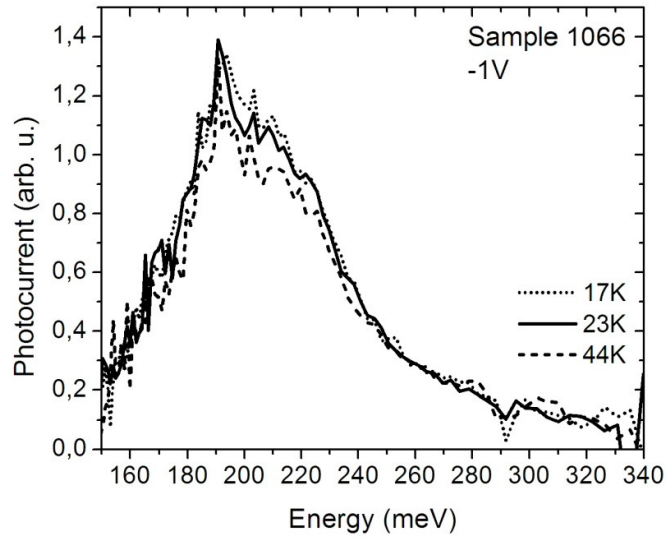Figure 5.19: Photocurrent of sample 1066 without bias at 19K.



Figure 5.20: Intraband photocurrent for different temperatures reverse biased with 1V (corrected by the source).
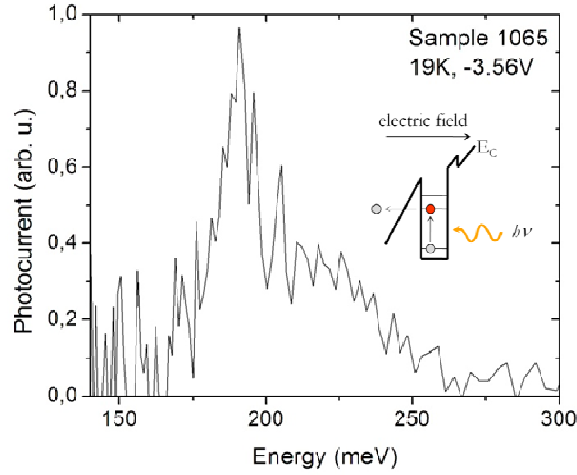
**Sample 1065**



Figure 5.21: Intraband photocurrent spectra for sample 1065 at 19K reverse biased with 3.56V corrected by the source. The inset shows the tunneling process at a high electric field.

The undoped sample 1065 is expected to generate no photocurrent due to the absence of carriers in the QD. Nevertheless due residual doping and carriers which are transferred from the contacts to the dot, intraband photocurrent can be measured. At low bias the signal is very weak, however reverse biasing it with 3.6V a photocurrent spectra is measured as can be seen in Figure 5.21. Due to the saturation of the used current preamplifier higher bias cannot be applied for this sample. At this high bias the conduction band gets strongly bent. One QD layer "sees" a potential difference around 356mV. In this case electrons can tunnel through the barriers and are collected by the electric field which can be seen in the inset of Figure 5.21.

The photocurrent spectrum of this sample is very narrow which indicates that QDs with a smaller size distribution are involved. The measurement is in good agreement with the FTIR result.

Intraband photocurrent measurements dependence on bias are performed. Due to the very weak signal of the undoped sample, polychromatic radiation was

used with an InAs filter to cut off wavelengths below 3.5µm. The corresponding spectrum is compared with the dark current at 19 K in Figure 5.22. As one can observe, both signals are very noisy between -1V and 1V due to device limitations in the measurement setup.



Figure 5.22: Photocurrent for polychromatic radiation in the intraband region and dark current versus bias voltage at 19K.

**Sample 1067**

Sample 1067 is highly doped and therefore the probability for intraband photocurrent is lower due to the absence of free excited states for intraband transition. The measured photocurrent spectrum is relatively broad and noisy. Figure 5.23 shows the photocurrent at 19K and reverse biased with 1.6V. The FTIR measurement showed a better result for this sample.
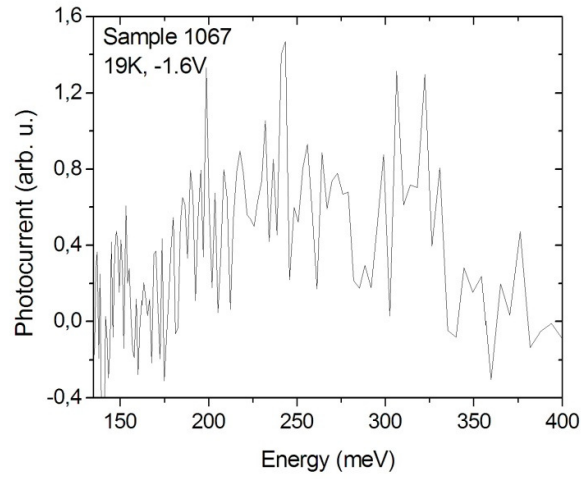
Figure 5.23: Intraband photocurrent spectra for sample 1067 at 19K reversed bias with 1.6V.

Intraband photocurrent using polychromatic radiation above 3.5μm compared with dark current at 19K is shown in Figure 5.24. The used current amplifier limits the current to a maximum of $10^{-7}$A. Higher bias voltage, as shown in the graph, cannot be applied without saturating the amplifier. The photocurrent at -1V is about 5 decades higher as compared with the photocurrent measurement with polychromatic radiation for sample 1065. This shows once more that the doping concentration is very high in this sample.
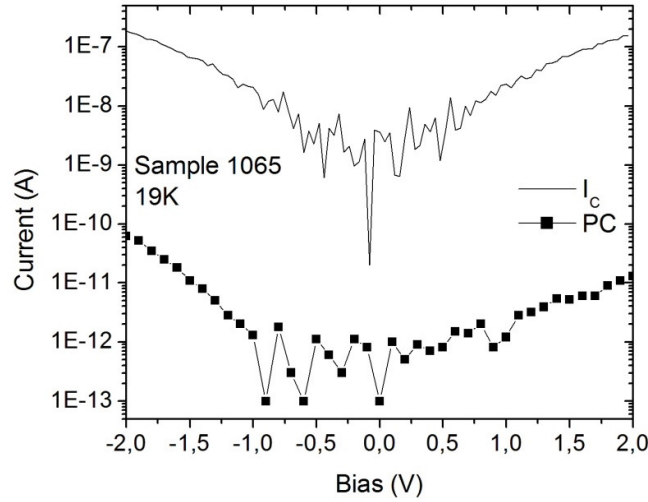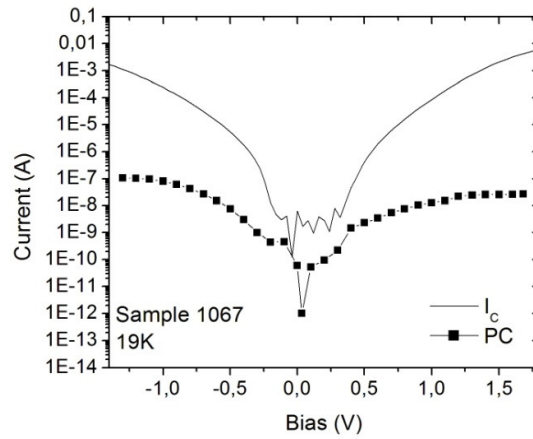
Figure 5.24: Photocurrent at polychromatic radiation in the intraband region and dark current versus bias voltage at 19K.

## Type B samples

The FTIR measurements of type B samples show a peak at 12μm, as mentioned previously. The potential output of the infrared lamp at 12μm is about one decade lower than at 6μm which can be seen from the spectral irradiance shown in Figure 4.5. The gratings working in the LWIR have also very low throughput. Without increasing the optical output of the current system it will be difficult to measure photocurrent in these samples. By using a special designed reflector a better efficiency in coupling in infrared radiation into the monochromator is expected. The current used standard reflector is working in such a way that part of the radiation is lost at the input. Further investigation has to be carried out.

# Chapter 6

# Summary and Outlook

In summary, QD structures for infrared photodetectors were investigated. To fully understand carrier dynamics in such complex structures appropriate characterization techniques are required. The investigation of QD structures detecting in the near infrared usually relies on intraband photocurrent measurements performed with FTIR spectroscopy. In this paper photocurrent measurement by monochromatic excitation was investigated to overcome the drawback of FTIR measurement techniques.

Three different doped samples based on InAs/InP QDs grown on InGaAlAs lattice matched to InP substrates showed a peak wavelength around 6.4µm. A lightly doped sample showed the best signal-to-noise ratio for the intraband photocurrent measurement. An undoped sample and a heavily doped sample showed a weak response, as one can expect. The obtained data gave further support that an intraband Auger effect is involved in generating the photocurrent.

This paper showed that the use of monochromatic excitation can be an important tool to analyze QD structures. Due to the relatively long measurement periods and the low optical throughput of this measurement technique, it is only suitable coexisting with FTIR spectroscopy. The optical output of the system could be increased by designing a special reflector to couple in more infrared radiation into the monochromator. A lamp working with higher optical power would also increase the output. It is expected, that with further investigation higher optical system throughput can lead to use this measurement technique also at longer wavelengths.

In general, QDIP have the potential to displace common state of the art infrared detectors, mainly HgCdTe. In my opinion, QDIP could be commercial available in between 5 to 10 years. By lowering the dark current higher operation temperatures will be achieved. Special blocking layers between QD structures, which filter dark current, but have no influence on the photocurrent, could lead to photodetectors working at room temperature. Without cooling QDIP could be miniaturized and available at low prices. The integration into other devices would be possible. A revolution in free space optical communication, toxic gas detection, and night vision cameras can be expected.

The reported results until now show a great potential of QDIP. But further investigations have to be done to design QDIP incorporating all the expected advantages.

# Bibliography

1. **Towe, E. and Pan, D.** Semiconductor Quantum-Dot Nanostructures: Their Application in a New Class of Infrared Photodetectors. *IEEE Journal of Selected Topics in Quantum Electronics.* 2000, 6,3, pp. 408-421.

2. **Krier, Anthony.** *Mid-infrared semiconductor optoelectronics.* s.l. : Springer, 2006.

3. **Finkman, E., Maimon, V., Immer, V., Bahir, G., Schacham, S.E., Gauthier-Lafaye, O., Herriot, S., Julien, F.H., Gendry, M. and Brault, J.** Quantum dot infrared photodetectors in new material systems. *Physica E 7.* 2000, S. 139-145.

4. **Liu, H.C.** Quantum dot infrared photodetector. *Opto-Electronics Review.* 2003, 11, 1, pp. 1-5.

5. **Rogalski, A.** Competitive technologies of third generation infrared photon detectors. *Opto-Electronics Review.* 2006, 14, 1, pp. 84-98.

6. **Ryzhii, V.** *Intersubband Infrared Photodetectors.* s.l. : World Scientific, 2003.

7. **Gebhard, T., Alvarenga, D., Souza, P.L., Guimarães, P.S.S., Unterrainer, K., Pires, M.P., Vieira, G.S. and Villas-Boas, J.M.** Intraband Auger effect in InAs/InGaAlAs/InP quantum dot structures. *Applied Physics Letters.* 2008, 93, 052103.

8. **Böberl, M., Kovalenko, M.V., Pillwein, G., Brunthaler, G. and Heiss, W.** Quantum dot nanocolumn photodetectors for light detection in the infrared. *Applied Physics Letters.* 2008, 92, 261113.

9. **Ishikawa, T., Nishimura, T., Kohmoto, S. and Asakawa, K.** Site-controlled InAs single quantum-dot structures on GaAs surfaces patterned by in situ electron-beam lithography. *Applied Physics Letters.* 2000, 76, 2, pp. 167-169.

10. **Fonseca Filho, H.D., Prioli, R., Pires, M.P., Lopes, A.S., Souza, P.L. and Ponce, F.A.** Growth of InAs nanostructures on InP using atomic-force nanolithography. *Applied Physics A.* 89, 2007, pp. 945-949.

11. **Schrey, F.F., Rebohle, L., Müller, T., Strasser, G., Unterrainer, K., Nguyen, D.P., Regnault, N., Ferreira, R. and Bastard, G.** Intraband transitions in quantum dot-supperlattice heterostructures. *Physical Review B 72.* 2005, 155310.

12. **Wang, S.Y., Lin, S.D., Wu, H.W. and Lee C.P.** Low dark current quantum-dot infrared photodetectors with an AlGaAs current blocking layer. *Applied Physics Letters.* 2001, 78, 8, pp. 1023-1025.

13. **Kim, E.T., Madhukar, A., Yee, Z. and Campell, J.C.** High detectivity InAs quantum dot infrared photodetectors. *Applied Physics Letters.* 2004, 84, 17, pp. 3277-3279.

14. **Lim, H., Tsao, S., Zhang, W. and Razeghi, M.** High-performance InAs quantum-dot infrared photodetectors grown on InP substrate operating at room temperature. *Applied Physics Letters.* 2007, 90, 131112.

15. **Barve, A.V., Shah, S.Y., Shao, J., Vandervelde, T.E., Shenoi, R.V., Jang, W.-Y. and Krishna, S.** Reduction in dark current using resonant tunneling barriers in quantum dots-in-a-well long wavelength infrared photodetector. *Applied Physics Letters.* 2008, 93, 131115.

16. **Tidrow, M.Z.** Multicolor Quantum Well Infrared Photodetectors. *Pentagon Reports.* 1998, A519553.

17. **Goldberg, A., Uppal, P.N. and Winn, M.** Detection of buried land mines using a dual-band LWIR/LWIR QWIP focal plane array. *Infrared Physics & Technology.* 2003, 44, pp. 427-437.

18. **Norton, P.** HgCdTe infrared detectors. *Opto-Electronics Review.* 10, 3, 2002, pp. 159-174.

19. **Majumdar, A., Choi, K.K., Reno, J.L., Rokhinson, L.P. and Tsui, D.C.** Two-color quantum-well infrared photodetector with voltage tunable peaks. *Applied Physics Letters.* 2002, 80, 5, pp. 707-709.

20. **Ma, W.Q., Yang, X.J., Chong, M., Yang, T., Chen, L.H., Shao, J., Lü, X., Lu, W., Song, C.Y. and Liu, H.C.** Voltage tunable two color InAs/GaAs quantum dot infrared photodetector. *Applied Physics Letters.* 2008, 93, 013502.

21. **Ariyawansa, G., Apalkov, V., Perera, A.G.U., Matsik, S.G., Huang, G. and Bhattacharya, P.** Bias-selectable tricolor tunneling quantum dot infrared photodetector for atmospheric windows. *Applied Physics Letters.* 2008, 92, 111104.

22. **Alsing, P.M., Cardimona, D.A., Huang, D.H., Apostolova, T., Glass, W.R. and Castillo, C.D.** Advanced space-based detector research at the Air Force Research Laboratory. *Infrared Physics & Technology.* 2007, 50, pp. 89-94.

23. **Systems, Raytheon Vision.** *Technology Today, Issue 1.* www.raytheon.com, 2008.

24. **Hoffmann, A.W., Love, P.L. and Rosbeck, J.P.** Mega-pixel detetcor arrays: visible to 28μm. *Proc. SPIE.* 2004, 5167, pp. 194-203.

25. **Gunapala, S.D., Bandara, S.V., Hill, C.J., Ting, D.Z., Liu, J.K., Rafol, S.B., Blazejewski, E.R., Mumolo, J.M., Keo, S.A., Krishna, S., Chang, Y.-C. and Shott, C.A.** Demonstration of 640x512 pixels long-wavelength infrared (LWIR) quantum dot infrared photodetector (QDIP) imaging focal plane array. *Infrared Physics & Technology.* 2007, 50, pp. 149-155.

26. **Phillips, J.** Evaluation of the fundamental properties of quantum dot infrared detectors. *Journal of Applied Physics.* 2002, 91, 7, pp. 4590-4594.

27. **Ustinov, V.M., Zhukov, A.E., Egorov, A.Y. and Maleev, N.A.** *Quantum Dot Lasers.* s.l. : Oxford Science Publications, 2003.

28. **Boucaud, P. and Sauvage, S.** Infrared photodetection with semiconductor self-assembled quantum dots. *C.R. Physique.* 2003, 4, pp. 1133-1154.

29. **Leonard, D., Krishnamurthy, M., Reaves, C.M., Denbaars, S.P. and Petroff, P.M.** Direct formation of quantum-sized dots from uniform coherent islands of InGaAs on GaAs surface. *Applied Physics Letters.* 1993, 63, pp. 3203-3205.

30. **Behet, M., Hövel, R., Kohl, A., Mesquida Küsters, A., Opitz, B. and Heime, K.** MOVPE growth of lll-V compounds for optoelectronic and electronic applications. *Microelectronics Journal.* 1996, 27, pp. 297-334.

31. **Bhattacharya, P., Krishna, S., Phillips, J., McCann, P.J. and Namjou, K.** Carrier dynamics in self-organized quantum dots and their application to long-wavelength sources and detectors. *Journal of Crystal Growth.* 2001, 227-228, pp. 27-35.

32. **Stiff-Roberts, A.D., Su, X.H., Chakrabarti, S. and Bhattacharya, P.** Contribution of Field-Assisted Tunneling Emission to Dark Current in InAs-GaAs Quantum Dot Infrared Photodetectors. *IEEE Photonics Technology Letters.* 2004, 16, 3, pp. 867-869.

33. **Kammerer, C., Sauvage, S., Fishman, G., Boucaud, P., Patriarche, G. and Lemaître, A.** Mid-infrared intersublevel absorption of vertically electronically coupled InAs quatum dots. *Applied Physics Letters.* 2005, 87, 173113.

34. **Liu, H.C., Gao, M., McCaffrey, J., Wasilewski, Z.R. and Fafard, S.** Quantum dot infrared photodetectors. *Applied Physics Letters.* 2001, 78, 1, pp. 79-81.

35. **Phillips, J., Kamath, K., Brock, T. and Bhattacharya, P.** Characteristics of InAs/AlGaAs self-organized quantum dot modulation doped field effect transistors. *Applied Physics Letters.* 1998, 72, 26, pp. 3509-3511.

36. **Nakaoka, T., Kako, S., Arakawa, Y. and Tarucha, S.** Coulomb blockade in a self-assembled GaN quantum dot. *Applied Physics Letters.* 2007, 90, 162109.

37. **Nakamura, Y., Ichikawa, M., Watanabe, K. and Hatsugai, Y.** Quantum fluctuation of tunneling current in individual Ge quantum dots induced by a single-electron transfer. *Applied Physics Letters.* 2007, 90, 153104.

38. **Borgstrom, M., Pires, M.P., Bryllert, T., Landi, S., Seifert, W. and Souza, P.L.** InAs quantum dots grown on InAlGaAs lattice matched to InP. *Journal of Crystal Growth.* 2003, 252, pp. 481-485.

39. **Carlsson, N., Junno, T., Montelius, L., Pistol, M.-E., Samuelson, L. and Seifert, W.** Growth of self-assembled InAs and InAsP dots on InP by metalorganic vapour phase epitaxy. *Journal of Crystal Growth.* 1998, 191, S. 347-356.

40. **Yoon, S., Moon, Y., Lee, T.-W. and Yoon, E.** Effects of As/P exchange reaction on the formation of InAs/InP quantum dots. *Applied Physics Letters.* 1999, Bd. 14, 74, S. 2029.

41. **Cornet, C., Schliwa, A., Even, J., Doré, F., Celebi, C., Létoublon, A., Macé, E., Paranthoën, C., Simon, A., Koenraad, P.M., Bertru, N., Bimberg, D. and Loualiche, S.** Electronic and optical properties of InAs/InP quatum dots on InP(100) and InP(311)B substrates: Theory and experiment. *Physical Review B 74.* 2006, 035312.

42. **Hwang, H., Park, K., Kang, J.-H., Ahn, E., Cheong, H.M. and Yoon, E.** Optical properties of InAs/InP quantum dot stack grown by metalorganic chemical vapor deposition. *Phys. State. Sol.* 2003, 4, pp. 1347-1350.

43. **Weber, A., Gauthier-Lafaye, O., Julien, F.H., Brault, J., Gendry, M., Désieres, Y. and Benyattou, T.** Strong normal-incidence infrared absorption in self-organized InAs/InAlAs quantum dots grown on InP (001). *Applied Physics Letters.* 74, 3, pp. 413-415.

44. **Sun, Q., Wang, Y.A., Li, L.S., Wang, D., Zhu, T., Xu, J., Yang, C. and Li, Y.** Bright, multicoloured light-emitting diodes based on quantum dots. *Nature Photonics.* 2007, 1, pp. 717-722.

45. **Marti, A. and Luque, A.** *Next Generation Photovoltaics.* s.l. : CRC Press, 2004. pp. 150-155.

46. **Mokerov, V.G., Fedorov, Y.V., Velikovski, L.E. and Scherbakova, M.Y.** New quantum dot transistor. *Nanotechnology.* 2001, 12, pp. 552-555.

47. **Oda, S. and Ferry, David K.** *Silicon Nanoelectronics.* s.l. : CRC Press, 2006. pp. 155-191.

48. **Macchiavello, Ch., Palma, G. M. and Zeilinger, A.** *Quantum Computation and Quantum Information Theory.* s.l. : World Scientific, 2000. pp. 425-440.

49. **Rogalski, A.** Infrared detectors: status and trends. *Progress in Quantum Electronics.* 2003, 27, pp. 59-210.

50. **Henini, M. and Razeghi, M.** *Handbook of Infrared Detection Technologies.* s.l. : Elsevier, 2002.

51. **Sze, S. M.** *Semiconductor Devices - Physics and Technology.* s.l. : Wiley, 2002. pp. 311-318. Vol. 2nd ed.

52. **Rogalski, A.** HgCdTe infrared detector material: history, status and outlook. *Reports on Progress in Physics .* 2005, 68, pp. 2267-2336.

53. **Levin, B. F.** Quantum-well infrared photodetectors. *J. Appl. Phys.* 74, 1993, pp. R1-R81.

54. **Schneider, H. und Liu, H.C.** *Quantum Well Infrared Photodetectors.* s.l. : Springer, 2006.

55. **Hsu, M.C., Chen, C.-C. and Kuan, C.-H.** Infrared Detection Utilizing Both Intersubband and Free-Carrier Absorption in Reverse-Biased Superlattice Infrared Photodetector. *IEEE Journal of Quantum Electronics.* 2003, 39, 11, pp. 1476-1480.

56. **Berryman, K.W., Lyon, S.A. and Segev, M.** Mid-infrared photoconductivity in InAs quantum dots. *Applied Physics Letter.* 1997, 70, 14, pp. 1861-1863.

57. **Müller, T., Schrey, F.F., Strasser, G. and Unterrainer, K.** Ultrafast intraband spectroskopy of electron capture and relaxation in InAs/GaAs quantum dots. *Applied Physics Letters.* 2003, 83, 17, pp. 3572-3574.

58. **Singh, Jasprit.** *Electronic and Optoelectronic Properties of Semiconductor Structures.* s.l. : Cambridge University Press, 2003.

59. **Souza, P. L., Lopes, A.J., Gebhard, T., Unterrainer, K., Pires, M.P., Villas-Boas, J.M., Vieira, G.S., Guimarães, and Studart, N.** Quantum dot structures grown on Al containing quarternary material for infrared photodetection beyond 10um. *Applied Physics Letters.* 2007, 90, 173510.

60. **Vurgaftman, I., Meyer, J.R. and Ram-Mohan, L.R.** Band parameters for lll-V compound semiconductors and their alloys. *Journal of Applied Physics.* 2001, 89, 11, pp. 5815-5875.

61. **Oriel, L.O.T.** 10-30W IR Sources. [Online] [Cited: 11 4, 2008.] http://www.lot-oriel.com.

62. **Hawkins, Gary J.** *Spectral Characterisation of Infared Optical Materials and Filters.* Thesis, Department of Cybernetics. s.l. : The University of Reading, 1998. p. 25.

63. **Mentges, Jochen.** *Call at LOT Oriel Germany.* 11 4, 2008.

64. **Asano, T., Madhukar, A., Mahalingam, K. and Brown, G.J.** Dark current and band profiles in low defect density thick multilayered GaAs/InAs self-assembled quantum dot structures for infrared detectors. *Journal of Applied Physics.* 2008, 104, 113115.

65. **Lim, H., Zhang, W., Tsao, S., Sills, T., Szafraniec, J., Mi, K., Movaghar, B. and Razeghi, M.** Quantum dot infrared photodetectors: Comparison of experiment and theory. *Physical Review B.* 2005, 72, 085332.

66. **Kang, Y.H., Park, J., Lee, U.H. and Hong, S.** Effect of the dot size distribution on quantum dot infrared photoresponse and temperature-dependent dark current. *Applied Physics Letters.* 2003, 82, 7, pp. 1099-1101.

# Detailed Description of the Samples

| Sample | B1 (nm) | QW (nm) | B2 (nm) | QD doping | B3 (nm) | Observations | |
|--------|---------|---------|---------|-----------|---------|--------------|---|
| 1065 | 109 | No | No | No | 16 | 152,6s B1 (InGaAlAs); 120s B3 (InP); 5,5s QD |  |
| 1066 | 109 | No | No | [Si]=12.4 sccm | 16 | Same as 1065 with doped QD | |
| 1067 | 109 | No | No | [Si]=25,4 sccm | 16 | Same as 1066 with higher doped QD | |
| 1068 | 99 | 10 | 3,0 | No | 16 | 138,6s B1 (InGaAlAs); 4,2s B2 (InGaAlAs); 140s B3 (InP); 14,2 s QW; 5,5s QD |  |
| 1069 | 99 | 10 | 3,0 | [Si]=12.4 sccm | 16 | Same as 1068 with doped QD | |
| 1070 | 99 | 10 | 3,0 | [Si]=25,4 sccm | 16 | Same as 1069 with higher doped QD | |

# Experimental Setup

**Used devices:**

- Low Noise Current Amplifier SR 570
- Lock in Amplifier SR 510
- Oriel Radiometric Power Supply 68931
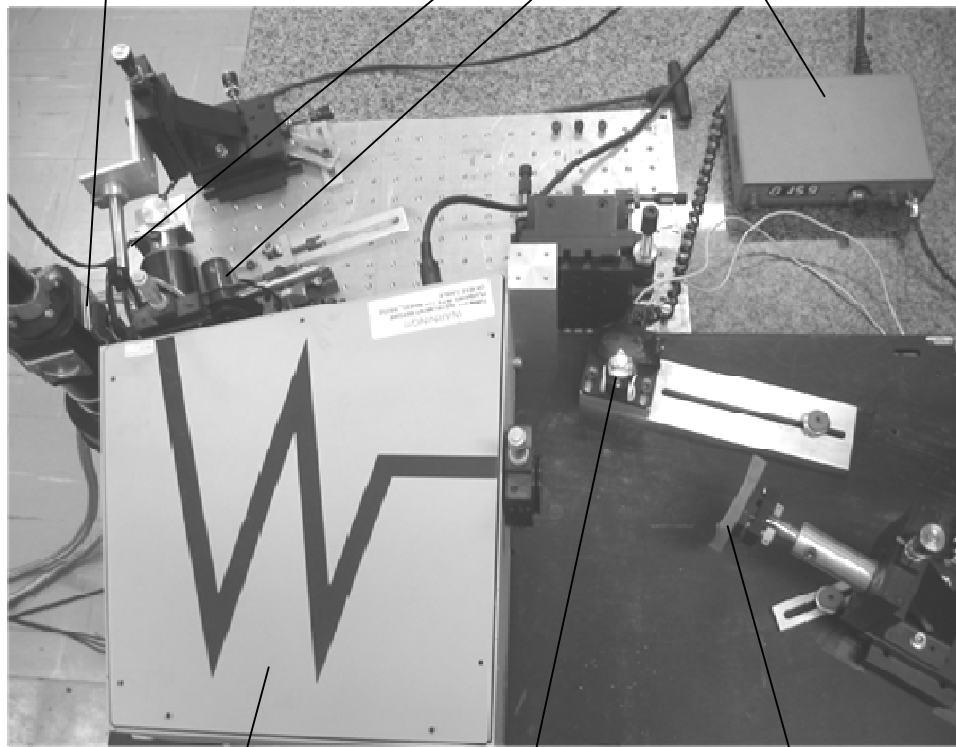- Oriel Lamp Housing 66881 (only for interband measurements)

Cryostat,
Leybold RDK 10-320
with InAs filter at input

Lens system

Optical Chopper and
Chopper Controller, SR 540



Oriel Cornerstone 260 1/4
Monochromator,
Model 74100

IR Lamp
LOT Oriel, LSB 151

AlMgF$_2$ Reflector
LOT Oriel, LSC095

# Acknowledgement

Gostaria de agradecer primero a minha orientadora no LabSem, Patrícia Lustoza de Souza e também aos novos amigos do LabSem pela ajuda durante todo o tempo e pela amizade.

Bedanken möchte ich mich bei Jürgen Smoliner, der mir ermöglicht hat, diese Arbeit in Brasilien durchzuführen.

Weiteres möchte ich mich bei Thomas Gebhard für die äußerst aufschlussreichen Diskussionen über das behandelte Themengebiet und für das Korrekturlesen der Arbeit bedanken.

Mein besonderer Dank gilt meinem Studienkollegen Martin Janits, für die vielen Tage des gemeinsamen Lernens während des Studiums, den gemeinsamen durchgeführten Projekten und besonders der uns verbindenden Freundschaft.

Bedanken möchte ich mich auch bei meinen Eltern, die mich während meiner gesamten Ausbildung immer unterstützt, mich jedoch niemals eingeschränkt und mir immer den nötigen Freiraum gelassen haben.